Rapid Remodeling of Human White Adipose Tissue Following Bariatric Surgery

Zinger Yang Loureiro[1]
Gregory P. Westcott[1,2]
Anton Gulko[1]
Adam Essene[1]
Zhibo Zhou[1]
Wenle Liang[1]
Christopher Jacobs[1]
Soumya Nagesh[1]
Nadejda Bozadjieva-Kramer[3,4]
Randy J. Seeley[3]
William Gourash[5]
Joseph J. Loureiro[6]
Lori L. Jennings[6]
Robert E. Gerszten[2,7]
Anita Courcoulas[5]
Linus T. Tsai[1,2]
Margo P. Emont[1,8,10]
Evan D. Rosen[1,2,9,10]

[1] Division of Endocrinology, Diabetes, and Metabolism, Beth Israel Deaconess Medical Center, Boston, MA, USA
[2] Harvard Medical School, Boston, MA, USA
[3] Department of Surgery, University of Michigan, Ann Arbor, MI
[4] Veterans Affairs Ann Arbor Healthcare System; Research Service; Ann Arbor, MI
[5] Department of Surgery, University of Pittsburgh Medical Center, Pittsburgh, PA, USA
[6] Novartis Biomedical Research, Cambridge, MA, USA
[7] Division of Cardiovascular Medicine, Beth Israel Deaconess Medical Center, Boston, MA, USA
[8] Biological Sciences Division, University of Chicago, Chicago, IL, USA
[9] Broad Institute of MIT and Harvard, Cambridge, MA, USA
[10] Corresponding authors: MPE (Margo.Emont@bsd.uchicago.edu); EDR (erosen@bidmc.harvard.edu)

Lead Contact: Evan Rosen (erosen@bidmc.harvard.edu)

Keywords: Adipose tissue; single cell; weight loss; bariatric surgery; hedgehog; Areg

SUMMARY

Bariatric surgery induces profound weight loss and improvement of obesity-associated metabolic dysfunction. Recent studies have shown that adipose tissue undergoes remodeling after weight loss, characterized by a reduction in proinflammatory immune cells, increased vascularization, and a shift in the adipocyte transcriptome, but these studies focused on time points long after surgery. We performed single nucleus RNA-seq (snRNA-seq) in subcutaneous white adipose tissue (SAT) samples from subjects with obesity undergoing bariatric surgery, collected at baseline and at one, six, and twelve months after surgery. We identify profound remodeling of SAT within the first month after surgery, characterized by a surge in lipid-associated macrophages and sharp reductions in specific populations of adipocytes, adipose stromal and progenitor cells (ASPCs), and endothelial cells. Transcriptional profiles strongly suggest that some adipocytes undergo apoptosis soon after surgery, while new adipocytes are generated by *de novo* differentiation. Mechanistically, the data are consistent with a model whereby coordinated early loss of a hedgehog signaling axis between endothelial cells and an anti-adipogenic population of ASPCs known as adipose regulatory cells (Aregs; $ASPC^{PTCH2}$) enables a transient burst of adipogenesis to occur. Interestingly, very few of these early features seen in human subjects are represented in a mouse model of surgical weight loss.

INTRODUCTION

Obesity, one of the most common medical conditions of the 21st century, is associated with a wide array of adverse health consequences, including type 2 diabetes (T2D), cardiovascular disease, and certain cancers, among others. Traditional approaches like dietary control and exercise have, in general, been unsuccessful in treating excess body weight. Until the recent development of drugs based on glucagon-like peptide 1 receptor (GLP1R) agonism, bariatric surgery was the only effective therapy for obesity. In fact, the weight loss-promoting effects of bariatric surgery may be longer lasting and more cost effective than even current forms of pharmacotherapy, and many patients still opt for bariatric surgery as a preferred option for weight loss.[1]

Adipose tissue comprises multiple cell types, including the major parenchymal cell type, the adipocyte. In addition, adipose tissue contains large numbers of adipose stromal and progenitor cells (ASPCs), vascular cells (blood and lymphatic endothelial cells, pericytes, and vascular smooth muscle cells), and both myeloid and lymphoid immune cells.[2,3] In addition, each of these major cell populations encompass several subpopulations, which differ in their gene expression patterns, and presumably in their

function as well. During the development of obesity, the composition of adipose tissue is altered, most notably reflecting the influx of proinflammatory immune cells.[4] In concert with these compositional changes, the metabolic activity of adipose tissue becomes deranged in the obese state. Studies in rodents and humans have pointed to several drivers of adipose dysfunction, including inflammation, activation of genes associated with senescence, oxidative and ER stress, and remodeling of extracellular matrix components.[5-7]

Significant weight loss, such as occurs after bariatric surgery, can rapidly restore insulin sensitivity, with many patients experiencing remission of T2D within days to weeks. Accordingly, there has been significant interest in assessing how weight loss affects the cellular composition and gene expression of adipose tissue. Three recent studies have described changes in human adipose tissue following bariatric surgery at single cell resolution, with all noting at least some degree of restoration of cellular composition and gene expression.[8-10] Notably, these studies are not fully concordant on some points, with some studies noting partial retention of obesity-associated features, while others suggest a more complete restoration to the original lean state. All published studies have focused on timepoints ranging from six to >24 months after bariatric surgery, long after metabolic function has been restored.

Here we report on the results of transcriptional profiling of subcutaneous white adipose tissue (SAT) from human subjects with obesity at single cell resolution before, and at one, six, and twelve months following bariatric surgery. We track cell populations and subpopulations that change over the time course of weight loss, and identify specific alterations that may impact metabolism. Most notably, our study identifies a large number of changes that occur in the first month following bariatric surgery, including a shift among adipocytes along two separate axes, suggesting simultaneous apoptosis of old, stressed adipocytes and their replacement through new differentiation of healthy cells. Moreover, we provide evidence that the process by which new adipogenesis is enabled is via the surgery-induced loss of a hedgehog signaling axis within the adipose niche involving a specific endothelial cell subpopulation and an anti-adipogenic population of ASPCs. Taken together, our data point to an extremely rapid and dynamic shift in adipose cellular composition and function early after bariatric surgery.

RESULTS

A longitudinal profile of subcutaneous adipose tissue after bariatric surgery

To determine the molecular changes in adipose tissue that follow bariatric surgery, we recruited 14 people with obesity, representing both sexes and diverse ages. These subjects were naive to GLP1 receptor agonists, and underwent either Roux-en-Y gastric

bypass (RYGB, n=7, 3 male, 4 female) or vertical sleeve gastrectomy (VSG, n=7, 4 male, 3 female). Abdominal SAT samples were collected during the initial surgery and at follow-up visits at one, six, and twelve months post-surgery (**Figure 1A**). All participants showed significant weight loss and metabolic improvement, including reduced Homeostasis Model Assessment of Insulin Resistance (HOMA-IR), within one month of the procedure (**Figures 1B, C** and **S1**).

We performed snRNA-seq on the 54 available tissue samples (two subjects were lost to follow-up at the 12 month timepoint), yielding transcriptomic profiles for 112,991 nuclei after filtering for quality control; all expected cell types in human SAT were identified (**Figures 1D** and **S2A**). We found no major differences in transcriptional profiles when comparing RYGB to VSG surgery, or between men and women (**Figures S2B-E**). Accordingly, subjects were pooled in subsequent analyses in order to maximize analytical power for our primary focus on differences across post-surgical timepoints.

Adipose tissue composition underwent major changes post-surgery, with many distinctive alterations observed at the earliest time points (**Figures 1D, E)**. At the one month mark, the immune cell component nearly doubled as a proportion of all cell types relative to baseline, before declining at the 6 and 12 month time points. This was especially striking as the doubling of the immune cell population coincided with the most robust improvements in HOMA-IR. In fact, while the proportion of immune cells correlated reasonably well with BMI across all time points (R^2 =0.180, p=0.001), there was no significant relationship between immune cells and HOMA-IR (R^2 =0.018, p=0.340) (**Figures 1F, G**). At one month, the proportion of adipocytes declined significantly, an effect partially attributed to extensive immune cell recruitment at that time point. By six and twelve months post-surgery, adipocyte proportions were comparable to baseline, in agreement with prior studies demonstrating that adipocyte number remains constant after weight loss.[11,12] Interestingly, the proportion of endothelial cells increased progressively following surgery. This increase was negatively correlated with both BMI and HOMA-IR, suggesting a potential link between improved adipose tissue vascularization and better overall metabolic health (**Figures S2F, G**).

As an orthogonal way to probe how these changes in adipose composition might affect systemic physiology, we connected our findings to changes in the plasma proteome using an independent dataset in which 4,151 proteins were profiled in the plasma of 35 non-diabetic adults at baseline, 1-2 months, and 6 months following RYGB.[13] All participants achieved significant weight loss (**Figure S3A**), and their plasma profiles were consistent with improved metabolism, including elevated SHBG and IGFBP isoforms (**Figure S3B**). Moreover, levels of well-known adipokines like leptin (encoded

by *LEP*) and adiponectin (encoded by *ADIPOQ*) decreased and increased, respectively, within 1-2 months (**Figure S3C**), consistent with their known behavior following weight loss. Also, in agreement with the snRNA-seq data, enrichment analysis of proteins significantly downregulated post-surgery indicated a marked decrease in inflammatory and immune responses and an increase in pathways associated with vascular development (**Figure S3D-G**).

Recruitment of lipid-associated macrophages immediately after bariatric surgery

To further characterize post-surgical immune profile changes, we subclustered the immune cell populations and assigned cell type based on marker gene expression (**Figures 2A, B**). Most immune cell types remained stable or slowly decreased in proportion after surgery (**Figures 2C-E**). A notable exception was a macrophage subpopulation marked by the fatty acid binding protein 4 (*FABP4*) gene. These cells, previously described as lipid-associated macrophages (LAM),[14] become significantly increased in representation one month after surgery, accounting for approximately 20% of all cells in the fat pad (**Figures 2C-E**). Histological evaluation of a representative donor revealed a striking, transient accumulation of crown-like structures surrounding adipocytes at one month post-surgery, which subsequently resolved by 6 and 12 months (**Figure 2F**). These cells, which possess a distinct capability for lipid handling, are marked by the triggering receptor expressed on myeloid cells 2 (*TREM2*) gene, as well as *IL1RN* (**Figure 2G, S4A)**. The plasma proteomic data was consistent with these results, showing that the LAM markers FABP4, TREM2 and IL1RN were transiently up-regulated in the blood at one to two months post-surgery (**Figure 2H**).

Increased vascularization accompanies the improvement of the metabolic profile

Our analysis identified all of the major vascular cell types in adipose tissue, including arterial, capillary, and venous blood endothelial cells, lymphatic endothelial cells, smooth muscle cells, and pericytes (**Figures 3A, B**). We noted progressive increases in the proportion of endothelial cells over the year following surgery, while lymphatic endothelial cells remained constant (**Figures 1E, 3C**), a finding corroborated by immunostaining (**Figure 3D**). As mentioned, this aligns with the plasma proteomic data, which showed an up-regulation of endothelial development pathways among circulating plasma proteins following bariatric surgery (**Figures S3F, G**). Notably, one subpopulation, denoted as Arterial^{PTPRJ} endothelial cells, decreased significantly after surgery (**Figures 3E, F**; discussed further below). The relative proportions of other arterial, venous, and capillary cells remain largely unchanged within the context of the overall expanding vasculature.

Adipocyte subpopulations shift dramatically soon after bariatric surgery

The spatial distribution of all adipose tissue cell types in the UMAP embedding suggested significant changes in the adipocyte profile following bariatric surgery (**Figure 1D**). To more finely characterize these changes, adipocytes were clustered into 10 subpopulations with distinct transcriptional profiles (**Figures 4A-C, S4B, C**). At baseline, Ad^{AKR1C2} and Ad^{CARD18} comprised the majority of adipocytes, but their representation significantly decreased by one month post-surgery and remained low thereafter (**Figure 4D**). Concurrently, the Ad^{VSTM4} population progressively expanded, comprising 59.2% of adipocytes at twelve months post-surgery (**Figure 4D**). Pathway analysis of markers indicates that Ad^{CARD18} likely represents 'stressed' adipocytes, with enrichment of pathways like the unfolded protein response (**Figure 4E**). Conversely, Ad^{VSTM4} markers are enriched in adipogenesis and glycerolipid biosynthesis pathway genes, suggesting that these represent healthier adipocytes (**Figure 4E**). Collectively, these data support the idea that adipocytes move from a biochemically stressed state in obesity to a more metabolically healthy profile by 6-12 months after surgery, consistent with prior observations.[8-10]

We noted the transient appearance of two subpopulations, Ad^{THBS1} and Ad^{SCD}, both of which showed highest representation at the one month timepoint (**Figure 4D**). Ad^{THBS1} adipocytes, which make up 27.4% of adipocytes at one month after surgery, exhibit markers enriched for 'apoptosis' and 'hypoxia' genes, suggesting that these represent adipocytes that may be in the process of being cleared from the tissue (**Figure 4F**). This is consistent with our observation that lipid-associated macrophages ($Macrophage^{FABP4}$) rise at one month post-surgery, as these cells have been implicated in clearing dead and dying adipocytes (**Figure 2C, D** and [15]). In contrast, Ad^{SCD} cells are enriched for markers of adipogenesis and fatty acid metabolism (**Figure 4F**). Given that the overall adipocyte proportion remains stable post-surgery (**Figure 1E**)[11,12], we speculate that Ad^{SCD} may represent newly developed adipocytes, although there is, to our knowledge, no specific transcriptional marker for a "young" adipocyte. Collectively, the contrasting profiles of Ad^{THBS1} (apoptosis/hypoxia) and Ad^{SCD} (adipogenesis/metabolism), alongside the elimination of Ad^{CARD18} (stressed) and establishment of Ad^{VSTM4} (healthy), provide evidence supporting a working model of adipocyte turnover following bariatric surgery in which at least some older, stressed adipocytes undergo cell death and are replaced by new, healthy adipocytes (**Figure 4G**).

Adipogenesis is detected after bariatric surgery

To further assess whether adipogenesis is heightened in the early phases of weight loss, we looked at the adipose stromal and progenitor cell (ASPC) population, which comprises a heterogeneous mesenchymal population with varying degree of adipogenic potential. Through subclustering, marker gene analysis and reference mapping, we identified known ASPC subtypes, including *DPP4*$^{+}$ early progenitor clusters

(ASPC$^{DPP4+,ABCB5+}$ and ASPC$^{DPP4+,ABCB5-}$), *PPARG*$^{+}$ committed preadipocyte clusters (ASPC$^{PPARG+,POSTN-}$ and ASPC$^{PPARG+,POSTN+}$), as well as ASPC^{PTCH2}, which most closely resembles a population of anti-adipogenic regulatory cells called Aregs (**Figures 5A-D, S4D, E**).[16,17]

Notably, ASPC$^{PPARG+,POSTN+}$ is a transient subpopulation observed almost exclusively at one month post-surgery (**Figure 5C, D**). These cells exhibit a transcriptional profile that is distinctive from other ASPC populations reported in this study and in the literature. ASPC$^{PPARG+,POSTN+}$ cells are characterized by the expression of transcription factors, including *RUNX1* and *RUNX2*, that are known for their role in mesenchymal development, as well as the adipogenic transcription factors *CEBPA* and *PPARG* (**Figure 5E**).[18-23] Furthermore, a subset of ASPC$^{PPARG+,POSTN+}$ cells distinctively express adipocyte marker genes such as *ADIPOQ*, *PLIN1*, and *LPL*, indicating they are differentiating progenitors actively acquiring adipocyte identity (**Figures 5E, F**). Analysis of the lineage trajectory shows that our data recapitulates the known ontogeny of adipogenesis, with *DPP4*$^{+}$ cells representing the earliest ASPCs, occurring earlier than ASPC$^{PPARG+,POSTN-}$ preadipocytes, which then diverge into non-adipogenic ASPC^{PTCH2} cells (Aregs) and ASPC$^{PPARG+,POSTN+}$ preadipocytes, the latter of which directly precedes the differentiated adipocyte state (**Figure S4F**). Collectively, these analyses corroborate the suggestion that active progenitor differentiation is most prominent at one month post-surgery.

Obesity upregulates anti-adipogenic hedgehog signaling, resolved with weight-loss

We next sought to identify processes that might account for increased adipogenesis following weight loss surgery. We noted that ASPC^{PTCH2} cells were significantly reduced in representation post-surgery (**Figure 5D**). This population most closely resembles cells identified by the Deplancke and Wolfrum group as adipogenic regulatory cells, or Aregs, which act to reduce adipogenesis (**Figure S4E**).[17] Review of ASPC^{PTCH2} markers and enrichment analysis revealed that they express genes associated with the hedgehog signaling pathway (**Figures 6A, B**), which is known for its role in developmental patterning and which has been shown to exert a strong anti-adipogenic effect.[24-27] It is known that adipogenesis is diminished in the obese state[28]; the relatively high proportion of ASPC^{PTCH2} cells could explain this, and their rapid decline following bariatric surgery might enable new adipogenesis.

ASPC^{PTCH2} cells have the machinery to respond to hedgehog proteins, but they do not produce the ligand themselves. We therefore looked across other cell types in the fat pad to see where hedgehog family members might be generated. Among the hedgehog ligands, only desert hedgehog (*DHH*) is expressed in adipose tissue, relatively

specifically by a subtype of arterial endothelial cells, Arterial^{PTPRJ} EC (**Figure 6C**). Following bariatric surgery, the proportion of this endothelial population and the expression of *DHH* both decreased, temporally correlating with the reduction in ASPC^{PTCH2} (**Figures 5D**, **6D, E** and **S5A**). Of note, Areg cells have been characterized as a perivascular stromal cell type,[17] consistent with current belief that hedgehog signaling acts in a paracrine manner over a short range. These findings are consistent with a model where direct signaling from endothelial *DHH*, specifically from the Arterial^{PTPRJ} EC population, promotes ASPC^{PTCH2}/Areg identity and/or function.

While our data highlights unique features of human adipose tissue remodeling, obtaining sufficient primary human ASPCs from this clinical cohort for mechanistic studies was not feasible. To test the idea that hedgehog signal promotes ASPC^{PTCH2}/Areg identity, we profiled the transcriptomes of primary mouse stromal vascular fraction (SVF) treated with either Smoothened receptor agonist (SAG) or recombinant human desert hedgehog (DHH), followed by bulk RNA sequencing. Treatment with these agonists up-regulated the expression of both hedgehog target genes and ASPC^{PTCH2} markers (**Figures 6F, G** and **S5B, C**). This effect on ASPC^{PTCH2} markers shows some specificity, in that genes that mark other ASPC populations are not up-regulated by hedgehog agonists (**Figures 6H** and **S5D**). Taken together, these data are consistent with a model in which endothelial-Areg hedgehog paracrine axis suppresses adipogenesis in the obese state, and becomes rapidly attenuated after bariatric surgery.

Senescence profiles improve following bariatric surgery, but follow different time courses in different cell types.

Senescence of many cell types in adipose tissue, including adipocytes, has been posited to drive metabolic deterioration in obesity, and recent reports suggest that bariatric surgery reduces adipose senescence.[9,29,30] We sought to determine whether this held true in our dataset. We first noted, however, that “senescence” gene sets differ greatly between published studies. We therefore took four recent gene sets purported to relate to senescence,[9,31-33] and focused on the nine genes that appeared in at least three of them (*CDKN1A*, *CDKN2A*, *TP53*, *CDK2*, *CDK6*, *ETS2*, *IGFBP7*, *IL1A*, and *IL6*) (**Figure S6A**). Adipocytes showed a steady and sequential decline in the core senescence marker gene expression across all timepoints. In contrast, in ASPCs, vascular, and immune cells, many senescence genes are actually elevated at the one month timepoint, before falling again at the 6 and 12 month timepoints (**Figures S6B, C**).

Lack of concordance between mouse and human adipose profiles after bariatric surgery

We have previously published a single cell analysis of white adipose tissue after VSG in mice,[34] which included early timepoints (10 and 35 days post-surgery), enabling us to compare the effect of bariatric surgery across species, with two important caveats. First, the mouse data do not represent serial samples on the same individual, as was done in the human. Second, by 35 days, mice with VSG had regained much of their lost weight, although they still weighed significantly less than the 35 day sham-operated control mice (**Figure 7A**). Spontaneous weight regain after VSG in mice has been noted by others as well.[35] With these caveats in mind, we identified similarities and differences in adipose tissue changes.

As expected, some of the changes that develop over 6-12 months in humans are not readily apparent in this short-term mouse experiment. For example, the overall proportion of vascular and immune cells remained unchanged after VSG in mice, in both inguinal and epididymal depots (rough orthologs of human SAT and visceral adipose tissue, respectively)(**Figure 7B**). Similarly, while genes associated with the unfolded protein response are prominent in adipocytes from obese mice, there is a mixed response to VSG, with some diminishing (e.g., *Cnot2*, *Dnajc3*) while others increase (e.g., *Exosc1*), often in a depot-specific manner (**Figure 7C**). The Ad^{VSTM4} markers, indicative of healthy, “destressed” adipocytes, are also not observed after VSG (**Figure 7D**).

The mouse data at the studied time points and depots do not, however, suggest that bariatric surgery induces an adipocyte turnover process analogous to what we observed in humans. Specifically, we observed no up-regulation of adipogenesis genes (indicated by Ad^{SCD} or Ad^{VSTM4} markers) or the emergence of an ortholog of $ASPC^{PPARG+,POSTN+}$ cells (**Figure 7D-F**). Similarly, while a few selected apoptosis and hypoxia genes that define human Ad^{THBS1} are expressed in adipocytes of obese mice, we do not see a response suggesting that apoptosis increases in either depot at the 10 day or 35 day timepoint (**Figure 7G**). This is concordant with the absence of $Macrophage^{FABP4}$/LAM expansion in the VSG group (**Figure S7H**), which may be required to police the adipose niche following adipocyte apoptosis.

Similar to the human data, we note that *Dhh* is the dominant hedgehog isoform in mouse adipose tissue, and that it is expressed in endothelial cells. *Dhh* expression is high in the inguinal adipose tissue of obese mice, and it diminishes after VSG (**Figure 7I**). Expression of hedgehog signaling genes in the ASPC population, however, shows a more mixed pattern with reduction of some genes (e.g., *Gli2*) and moderate increases in *Ptch2* (**Figure 7J**). Contrary to what we noted in humans, the Areg population in mouse

adipose tissue (identified as mASPC4 in our prior mouse work) increases with weight loss in all depots and time points tested (**Figure 7K, L**).

DISCUSSION

In this study, we provide a longitudinal characterization of the cellular changes in human SAT during bariatric surgery-induced weight loss. By tracking the same patient cohort over a one-year period, we were able to observe the tissue as it transitioned from a state of obesity-associated metabolic stress to a post-weight-loss healthier steady state. Our data demonstrate significant shifts in the transcriptional identity and proportions of nearly every major cell type within the adipose niche. While other single-cell studies have described the adipose landscape in response to surgically-induced weight loss,[8-10] our study is unique in capturing the early one month post-operative time point. This window enabled us to see early changes during a phase of remodeling that correlates temporally more closely with improvements in metabolic function. One obvious illustration of the power of this approach is our observation that the long-term decrease in immune cell infiltration reported by others (and seen by us at later timepoints) is preceded by a transient upregulation of Macrophage^{FABP4}/LAMs at one month. As discussed below, we speculate that this early response may be essential for the clearance of apoptotic, lipid-laden adipocytes and the initiation of healthy tissue turnover. Lipid-associated macrophages have been linked to obesity-associated insulin resistance[36]; in contrast, we note that the transient elevation in these cells in SAT following bariatric surgery was temporally associated with profoundly improved HOMA-IR.

There is also a complex relationship between body weight and adipose vascularity. In general, obesity is considered to drive relative hypoxia in the fat pad, which raises VEGF expression in adipocytes and in plasma.[37-39] Whether this leads to increased vascularity in obesity is unclear, however. Single cell data from lean and obese human adipose tissue suggest a lower proportion of endothelial and other vascular cell types in samples from obese vs. lean subjects; this is in line with deconvoluted bulk RNA-seq data from the METSIM cohort.[40,41] In contrast, little is known about the response of the adipose vasculature to weight loss. Lower vascular density has been correlated with more robust weight loss after bariatric surgery, but this study used samples collected at the time of surgery and did not follow vascularity over time.[42] A recent study by the Mandrup group indicates that vascularity increases in SAT after bariatric surgery,[10] which we also observe.

In both humans and mice, adipocytes in the obese state exhibit signs of stress, with up-regulation of genes associated with hypoxia,[43] inflammation,[44] and insulin resistance,[45]

seen also in our baseline samples. By the 6-12 month post-surgical timepoints, the gene expression pattern of adipocytes has shifted dramatically, with up-regulation of fatty acid metabolic genes and other hallmarks of healthy adipocytes. What accounts for the presence of these healthy adipocytes after weight loss? Do they represent older adipocytes that have 'de-stressed', or are they new adipocytes that differentiated following the surgical intervention? If the latter, what has become of the older, stressed fat cells? Our transcriptional study cannot definitively answer these questions, but at one month following surgery, we note that the adipocyte compartment exhibits evidence of two separate processes: apoptosis of older, stressed adipocytes and the simultaneous formation of new, healthy fat cells.

Healthy adipocytes are relatively resistant to apoptosis, in part because of insulin action, and also because they express many anti-apoptotic factors.[46] Obesity, however, is associated with enhanced apoptosis of adipocytes, with dead and dying fat cells surrounded by a corona of pro-inflammatory macrophages called a crown-like structure.[15,47] Interestingly, blockade of adipocyte apoptosis through targeted deletion of caspases or other proapoptotic factors prevents excess weight gain on high fat diet and reduces adipose inflammation and insulin resistance.[47-50] Our data suggest that rather than relieve this apoptotic state, the early stages of weight loss are characterized by enhanced adipocyte death. One subpopulation of adipocytes (Ad^{THBS1}) is notable for its expression of pro-apoptotic genes, including *VDAC2*,[51,52] *TGFBR3*,[53] *ANXA1*,[54] *DAP*,[55] and *IRF1*.[56] These cells represent approximately 15% of subcutaneous adipocytes at baseline, and then increase in abundance after surgery, accounting for roughly 30% of adipocytes at one month. They then diminish over time, representing <5% of adipocytes by 1 year post-surgery. These data suggest that one possible fate of the stressed adipocyte, even after the energy imbalance that caused obesity is rectified, is death. This is consistent with the increased number of $Macrophage^{FABP4}$/LAMs at one month, which may be required to clean up cellular debris and free lipid following apoptosis.

In both rodents and humans, the number of small adipocytes increases after weight loss.[10,57-59] We speculate that some of this reflects delipidation of larger fat cells, but there may also be a role for new adipogenesis. Unfortunately, there is no definitive gene expression marker for a "young" adipocyte. Nevertheless, at 1 month post-surgery we note the appearance of a subpopulation of adipocytes marked by *SCD*. These cells express genes characteristic of adipogenesis. By the 6 month timepoint, these cells have largely returned to their lower baseline levels. Concordant with the appearance of these adipocytes, there is the emergence of a population of ASPCs (*PPARG*+,*POSTN*+) that express adipocyte genes such as *PLIN1*, *ADIPOQ*, and *LPL*. Taken together, our data support the notion that there is a wave of new adipogenesis at the one month timepoint that dissipates before 6 months.

Our data are consistent with a small body of literature suggesting that precursor cells isolated from individuals with obesity exhibit reduced adipogenic potential.[60,61] This diminished adipogenic capacity has been proposed to contribute to the hypertrophy of existing adipocytes; hypertrophic adipocytes are in turn believed to be most active in promoting the metabolic dysfunction associated with obesity.[62] Moreover, adipose precursor cells isolated after weight loss (induced by dietary restriction) demonstrate improved adipogenic potential *in vitro*.[63]

Mechanistically, how might adipogenesis be repressed in obesity, and then reactivated after weight loss? Our attention was drawn to a population of ASPCs known as Aregs (identified as $ASPC^{PTCH2+}$ in our study), which exert anti-adipogenic actions on neighboring cells,[17] and which decrease in abundance shortly after surgery. Notably, these cells are characterized by expression of several hedgehog receptors and signaling intermediates. Moreover, we show that *in vitro* treatment of mouse ASPCs with hedgehog agonists promotes Areg identity. We acknowledge the inherent limitation of using a murine *in vitro* system to validate a pathway identified in human tissue, particularly given that our *in vivo* mouse VSG model does not perfectly mirror the Areg population dynamics observed in humans. Nevertheless, the conserved capacity of these progenitor cells to upregulate Areg markers in response to hedgehog ligands *in vitro* provides plausible mechanistic support for the endothelial-Areg signaling axis proposed by our human transcriptomic data. Hedgehog signaling is recognized to inhibit white adipocyte differentiation in flies,[26,64] mice,[26] and human cells[65]; this effect is believed to involve direct actions on precursor cells, at least in culture. While we do see some hedgehog receptor expression on adipose progenitor (in particular $ASPC^{PPARG+POSTN-}$) cells, this is dwarfed by expression on $ASPC^{PTCH2+}$ Aregs. While Aregs respond to hedgehog signaling, they do not produce any of the recognized hedgehog ligands. Indeed, the DePlancke and Wolfrum groups identified several non-hedgehog paracrine factors (e.g., *Rtp3*, *Spink2*, *Fgf12* and *Vit*) as possible mediators of the anti-adipogenic action of Aregs.[17]

Where then, is hedgehog produced in the human adipose niche? Our data show that only one hedgehog ligand, desert hedgehog (DHH), is found in human adipose tissue, and that it is expressed exclusively by blood endothelial cells, specifically, a unique subpopulation of endothelial cells identified as $Arterial^{PTPRJ}$ ECs. These cells rapidly decline following bariatric surgery, accompanied by reductions in *DHH* mRNA levels and immunostaining. In other contexts, DHH is involved in the response to injury.[27,66] Specifically, muscle injury triggers the activation of fibro-adipogenic progenitors, wherein DHH is upregulated to repress fat deposition and improve muscle healing.[27] In this light, DHH expression in obesity may represent a maladaptive injury response that

prevents healthy adipose tissue homeostasis. Alternatively, DHH expression and signaling may be responding to local hypoxia in obese SAT, as hedgehog has been implicated in angiogenesis and the development of arterial endothelial cells.[67-69] Of note, Areg cells localize to the perivascular space,[17] consistent with the known range of hedgehog signaling as a short-range paracrine mechanism.[25,70,71]

Prior reports suggest that senescence is a driver of metabolic dysfunction in obesity, and a recent study indicates that the expression of senescence-associated genes becomes attenuated after weight loss surgery.[9] Our data supports this idea, but a few points bear mentioning. First, there is little consensus among published gene sets about which markers truly represent markers of senescence. We tried to mitigate this issue by focusing only on genes that were included in at least three out of four published gene sets. Second, all major cell types in SAT express these 'consensus' senescence markers at high levels in the obese state, with diminution occurring over the 12 month course of the study period. However, only adipocytes show a stepwise reduction in the expression of these genes - the other major cell types (ASPCs, vascular, and immune cells) all display elevated senescence gene expression at the one month timepoint. It is unclear why this should be so, but one possible explanation is that these cells are exposed to the contents of apoptotic adipocytes, which induce metabolic stress and drive senescence.

We recently performed an analysis of adipose tissue composition following VSG in mice,[34] allowing us to draw cross-species comparisons, with caveats discussed earlier. Of note, we did not detect changes in the relative amounts of vascular or immune cells in the WAT of mice after either VSG or semaglutide-mediated weight loss. This may reflect true differences between species, or perhaps the much shorter time course assessed in the mouse vs. human studies (1 month vs. 6-12 months). When assessing alterations noted at 1 month in humans, we see that there are some common features, notably elevated expression of *Dhh* in endothelial cells at baseline, which goes down following surgery in both species. We do not, however, see evidence of apoptosis of existing adipocytes, nor differentiation of new adipocytes in the first month after surgery, nor reductions in Areg levels. One interesting possibility is that failing to purge the adipose niche of large, stressed adipocytes might predispose to weight regain. Further experimentation is required to delineate why these differences exist and whether they have implications for surgical outcomes in either species.

Limitations of the Study

Our study has several limitations. First, even though we report data from the earliest post-surgical time point yet, metabolic function had already improved significantly. Our

study thus lacks the resolution to determine the precise temporal relationship between the changes in cellular composition and metabolic benefit. Second, our study was limited to SAT, due to its accessibility in an outpatient setting. We do not know whether the changes we observe in SAT are reflected in other depots, particularly omental adipose tissue. Third, a comparator group that lost weight without surgery, such as through lifestyle intervention or GLP1R agonists, would have been interesting. Lifestyle changes tend to reduce weight only a small amount and less durably, however. Finally, perhaps the most important limitation is that we can only draw inferences about the biological processes actually occurring in the adipose tissue after weight loss from changes in gene expression. There is no way, for example, to measure adipogenesis in real time in living human subjects.

ACKNOWLEDGEMENTS

This work was supported by NIH RC2 DK116691 to EDR and NIH K01 DK134806 to MPE. We thank the Functional Genomics and Bioinformatics Core at BIDMC (supported by P30 DK135043). We thank members of the Rosen lab for helpful discussions.

AUTHOR CONTRIBUTIONS

Experimental Design: MPE, EDR
Experimental Execution: ZYL, MPE, GPW, AG, AE, ZZ, WL, LTT
Sample Collection: WG, AC, NBK, RJS
Data Analysis: ZYL, MPE, GPW, CL, SN, JJL, LLJ, REG, EDR
Manuscript Preparation: ZYL, MPE, GPW, EDR
Supervision and Funding: EDR

DECLARATION OF INTERESTS

EDR is on the Scientific Advisory Board of Source Bio, Inc. RJS has received research support from Fractyl, AstraZeneca, Congruence Therapeutics, Eli Lilly, Diasome, and Amgen. RJS has served as a paid consultant for Novo Nordisk, Eli Lilly, CinRx, Crinetics, Amgen, Helicore, Gallant, General Medicines, Abbvie, Protagonist Therapeutics, Aardvark, Zealand, Alveus and Nuanced Health. RJS holds equity in Nuanced Health, Coronation Bio, Eccogene, Fractyl, and Rewind. JJL and LLJ are employees of Novartis.

FIGURE LEGENDS

Figure 1. The composition of human adipose tissue changes early after bariatric surgery

(A) Overview of the study design.

(B) Body mass index (BMI) of participants following surgery, grouped by procedure (left panel) and sex (right panel). Thin colored lines represent individual participants; thick lines and data points indicate aggregated results across participants.

(C) Homeostatic Model Assessment of Insulin Resistance (HOMA-IR) of participants following surgery, grouped by procedure (left panel) and sex (right panel). Thin colored lines represent individual participants; thick lines and data points indicate aggregated results across participants.

(D) Uniform manifold approximation and projection (UMAP) of snRNA-seq data from adipose tissues of 14 donors, split by timepoint. A total of 112,991 nuclei passed quality filtering, and plots were down-sampled to 15,997 nuclei per timepoint for visual comparison. Colors indicate major cell types.

(E) Relative proportions of major cell types at designated timepoints. Data are represented as mean ± SEM. Statistical significance of variations in cell type proportions across different timepoints was assessed using the propeller method implemented in R package speckle.

(F) The relationship between the proportion of immune cells and the corresponding donor's BMI at the time of sampling. Individual participants are differentiated by point shape, and different timepoints are indicated by color.

(G) The relationship between the proportion of immune cells and the corresponding donor's HOMA-IR score at the time of sampling. Individual participants are differentiated by point shape, and different timepoints are indicated by color.

Figure 2. Changes in immune cell classes in SAT after bariatric surgery

(A) UMAP projection of 28,136 immune cells.

(B) Expression of immune cell type markers.

(C) UMAP projections of immune populations, separated by sampling timepoint. Each plot is normalized to an equal cell count (n = 1,979), with 2D density contours overlayed.

(D) Relative proportions of immune cell types as a percentage of all adipose tissue cells across timepoints. Data are represented as mean ± SEM. Statistical significance of variations in cell type proportions across different timepoints was assessed using the propeller method implemented in R package speckle.

(E) Relative proportions of immune cell types as a percentage of all immune cells across timepoints. Data are represented as mean ± SEM. Statistical significance of variations in cell type proportions across different timepoints was assessed using the propeller method implemented in R package speckle.

(F) Representative haematoxylin and eosin staining of SATs from a single donor. Scale bar, 100 μm.

(G) Expression of *IL1RN* and *TREM2* genes (associated with Macrophage^{FABP4}) in SAT following surgery. Data are presented as log2-transformed counts per million. Statistical significance was determined via the Quasi-Likelihood F-test.
(H) Levels of IL1RN and TREM2 proteins in plasma after bariatric surgery (n = 35 subjects). Repeated measures ANOVA was used to evaluate statistical significance. Data distribution shown via violin plots (mean ± 95% bootstrapped CI).

Figure 3. Changes in vascular cell classes in SAT after bariatric surgery
(A) UMAP projection of 27,874 vascular cells.
(B) Expression of vascular cell type markers.
(C) Relative proportions of vascular cell types as a percentage of all adipose tissue cells across timepoints. Data are represented as mean ± SEM. Statistical significance of variations in cell type proportions across different timepoints was assessed using the propeller method implemented in R package speckle.
(D) Representative immunofluorescence staining for CD31 expression. Scale bars, 100 µm.
(E) UMAP projections of vascular cell populations, separated by sampling timepoint. Each plot is normalized to an equal cell count (n = 5,844), with 2D density contours overlayed.
(F) Relative proportions of vascular cell types as a percentage of all vascular cells across timepoints. Data are represented as mean ± SEM. Statistical significance of variations in cell type proportions across different timepoints was assessed using the propeller method implemented in R package speckle.

Figure 4. Changes in adipocyte subtypes in SAT after bariatric surgery
(A) UMAP projection of 29,033 adipocytes.
(B) Expression of adipocyte subtype markers.
(C) UMAP projections of adipocyte populations, separated by sampling timepoint. Each plot is normalized to an equal cell count (n = 4,183), with 2D density contours overlayed.
(D) Relative proportions of adipocyte subtypes as a percentage of the overall adipocyte population across timepoints. Data are represented as mean ± SEM. Statistical significance of variations in cell type proportions across different timepoints was assessed using the propeller method implemented in R package speckle.
(E) Expression of genes associated with the “unfolded protein response”, “adipogenesis”, and “glycerolipid biosynthesis” pathways in each adipocyte subtype.
(F) Expression of genes associated with the “apoptosis”, “hypoxia”, “adipogenesis” and “fatty acid metabolism” pathways in each adipocyte subtype.
(G) Proposed model of adipocyte turnover dynamics in SAT following bariatric surgery.

Figure 5. Subclustering of adipose stromal and progenitor cells (ASPCs)
(A) UMAP projection of 27,948 ASPCs.
(B) Expression of ASPC cell type markers.
(C) UMAP projections of ASPC populations, separated by sampling timepoint. Each plot is normalized to an equal cell count (n = 2,890), with 2D density contours overlayed.
(D) Relative proportions of ASPC subtypes as a percentage of the overall ASPC cell population across timepoints. Data are represented as mean ± SEM. Statistical significance of variations in cell type proportions across different timepoints was assessed using the propeller method implemented in R package speckle.
(E) Expression of selected $ASPC^{PPARG+,POSTN+}$ markers.
(F) UMAP projection of ASPCs colored by expression of adipocyte markers.

Figure 6. Anti-adipogenic hedgehog signals diminish after bariatric surgery
(A) Expression of hedgehog pathway genes in ASPC subtypes.
(B) Expression of hedgehog pathway genes in SAT over the course of this study. Data are presented as log2-transformed counts per million. Statistical significance was determined via the Quasi-Likelihood F-test.
(C) Expression of hedgehog ligands in all SAT cell subtypes.
(D) Expression of *DHH* across timepoints. Data are presented as log2-transformed counts per million. Statistical significance was determined via the Quasi-Likelihood F-test.
(E) Quantification of the percentage of DHH^{+} vessels performed on adipose tissues from three individuals at four post-surgical time points. Each data point represents the aggregate average calculated from five images acquired from the corresponding tissue sample. Bar plot data are represented as mean ± SEM. Repeated-measures ANOVA was used to assess statistical significance.
(F) Expression of hedgehog pathway genes in primary mouse stromal vascular fraction (mSVF) treated with 200 nM of SAG or vehicle for 24 hours (n=3 per treatment condition). Bar plot data are represented as mean. Statistical significance was assessed using the Wald test implemented in the DESeq2 R package.
(G) Expression of $ASPC^{PTCH2}$ markers in mouse SVF treated with 200 nM of SAG or vehicle for 24 hours (n=3 per treatment condition). Bar plot data are represented as mean. Statistical significance was assessed using the Wald test implemented in the DESeq2 R package.
(H) Enrichment analysis using a hypergeometric test performed on genes differentially upregulated in mSVF treated with 200 nM SAG, compared to vehicle treatment. The gene sets used for this analysis were based on markers for ASPC subtypes.

Figure 7. Findings in human adipose tissue post-bariatric surgery are only partially mirrored in the bariatric surgery mouse model
(A) The percent weight changes in mice following either VSG or sham surgeries, with data sourced from Emont, et al. Error bars represent the standard error. Statistical significance was assessed using a student's *t*-test to compare the body weights of the VSG and sham groups, with correction for multiple comparisons applied via a false discovery rate (FDR). *FDR < 0.05.
(B) Relative proportions of major cell types in mouse epididymal (EPI) or inguinal (ING) adipose tissue at designated timepoints after VSG.
(C) Expression of the unfolded protein response related genes that were observed in human Ad^{CARD18}, in mouse adipocytes after VSG.
(D) Expression of adipogenesis and glycerolipid biogenesis related genes that were observed in Ad^{VSTM4}, in mouse adipocytes after VSG.
(E) Expression of adipogenesis and fatty acid metabolism related genes that were observed in Ad^{SCD}, in mouse adipocytes after VSG.
(F) Expression of $ASPC^{PPARG+,POSTN+}$ markers in mouse ASPCs after VSG.
(G) Expression of apoptosis and hypoxia genes, observed in Ad^{THBS1}, in mouse adipocytes after VSG.
(H) Expression of Mac^{TREM2} markers in the immune cells of mouse adipose tissue after VSG.
(I) Expression of Hedgehog ligands in the vascular cells of mouse adipose tissue after VSG.
(J) Expression of Hedgehog pathway genes in mouse ASPCs after VSG.
(K) Expression of Hedgehog pathway genes in mouse ASPC subtypes.
(L) Relative proportion of mASPC4/Areg in EPI or ING adipose tissues at designated timepoints after VSG.

SUPPLEMENTAL FIGURES

Figure S1. Demographic characteristics and metabolic characterization of bariatric surgery weight loss study participants across timepoints, related to main Figure 1
F = female, M = male, yo = year-old, AA = African American.

Figure S2. Major cell types in SAT, related to main Figure 1
(A) Expression of broad cell type markers in human SAT.
(B) UMAP projections of major cell types in SAT, separated by surgery type. Each plot is normalized to an equal cell count (n = 54,048).
(C) Stacked bar plot depicting cell-type composition of each adipose tissue sample, grouped by surgery type and timepoint. Colors reflect cell types in (B).

(D) UMAP projections of adipose tissue major cell types, separated by sex. Each plot is normalized to an equal cell count (n = 56,405).
(E) Stacked bar plot depicting cell-type composition of each adipose tissue sample, grouped by sex and timepoint. Colors reflect cell types in (D).
(F) The relationship between the proportion of each major cell type and the corresponding donor's BMI at the time of sampling. Individual participants are differentiated by point shape, and different timepoints are indicated by color.
(G) The relationship between the proportion of major cell types and the corresponding donor's HOMA-IR score at the time of sampling. Individual participants are differentiated by point shape, and different timepoints are indicated by color.

Figure S3. Longitudinal plasma proteomic profiling of bariatric surgery patients, related to main Figures 2 and 3
(A) BMI of SomaScan plasma proteomic study participants following surgery, grouped by sex. The analysis for this manuscript was restricted to the subset of participants who were non-diabetic and had data available across all three study timepoints (n=35). Thin colored lines represent individual participants; thick lines and data points indicate aggregated results across participants.
(B) Levels of plasma proteins that reflect participants' insulin sensitivity after bariatric surgery. Repeated measures ANOVA was used to evaluate statistical significance. Data distribution shown via violin plots (mean ± 95% bootstrapped CI).
(C) Levels of plasma adiponectin (ADIPOQ) and leptin (LEP) after bariatric surgery. Repeated measures ANOVA was used to evaluate statistical significance. Data distribution shown via violin plots (mean ± 95% bootstrapped CI).
(D) Downregulated inflammatory pathway following bariatric surgery, derived from the list of all significantly downregulated plasma proteins.
(E) Levels of plasma proteins associated with inflammatory pathways following bariatric surgery. Repeated measures ANOVA was used to evaluate statistical significance. Data distribution shown via violin plots (mean ± 95% bootstrapped CI).
(F) Upregulated vascular development pathways following bariatric surgery, derived from the list of all significantly upregulated plasma proteins.
(G) Levels of plasma proteins associated with vascular development following bariatric surgery. Repeated measures ANOVA was used to evaluate statistical significance. Data distribution shown via violin plots (mean ± 95% bootstrapped CI).

Figure S4. Adipocyte and ASPC subtypes, related to main Figures 4 and 5
(A) Expression of lipid handling genes among Macrophage^{FABP4} markers in immune cells.

(B) Riverplot depicting the adipocyte subtype labels used in this manuscript, mapped to the corresponding cell types identified in human SAT adipocyte nuclei from Emont, et al.
(C) Expression of genes associated with “transcription”, “adipokine secretion”, “insulin signaling”, “lipid handling”, and “thermogenesis” pathways across adipocyte subtypes.
(D) Riverplot depicting the ASPC subtype labels used in this manuscript, mapped to the corresponding cell types identified in human SAT ASPC nuclei data from Emont, et al.
(E) Expression of Areg marker genes reported by Schwalie, et al. and selected $ASPC^{PTCH2}$ markers across ASPC subtypes.
(F) Lineage structure of ASPC subtypes progressing to adipocytes. Each node contains a pie chart that illustrates the relative abundance of each ASPC subtypes at each timepoint, specifically depicting the percentage of each subtype within the total ASPC cell population.

Figure S5. Hedgehog signaling defines $ASPC^{PTCH2}$ identity, related to main Figure 6

(A) Immunofluorescence staining for DHH and pan-endothelial marker CD31 in SAT following bariatric surgery. Scale bar, 100 μm.
(B) Expression of hedgehog pathway genes in primary mouse SVF treated with 1 μg/mL of recombinant DHH or vehicle for 24 hours.
(C) Scatter plot comparing gene expression changes (log2 fold changes) between SAG- and vehicle-treated cells with those between DHH- and vehicle-treated cells. This plot serves to identify common upregulated signals across the two experiments, with specific highlighting of genes associated with the hedgehog pathway.
(D) Scatter plot comparing gene expression changes (log2 fold changes) between SAG-treated and vehicle-treated cells with those between DHH-treated and vehicle-treated cells. Marker genes for each ASPC subtype were highlighted in each plot. The background color in each quadrant of the plot reflects the proportion of subtype marker genes found within that respective quadrant.

Figure S6. Turnover of senescent adipocytes accompanies metabolic improvement

(A) Venn diagram showing the overlap of genes derived from four distinct senescence gene sets; see text for details.
(B) Expression of core senescence-associated genes in major cell types across timepoints.
(C) Expression of core senescence-associated genes across cellular subtypes.

.

KEY RESOURCES TABLE

REAGENTS OR RESOURCES	SOURCE	IDENTIFIER
Antibodies		
DHH (1:100)	Thermo Fisher Scientific	PA5-115118
CD31 monoclonal antibody, Alexa Fluor 488 (1:100)	Thermo Fisher Scientific	MA5-18135
Alexa Fluor 647 donkey anti-rabbit (1:250)	Thermo Fisher Scientific	A-21447
Hoechst 33342 (1:1000)	Thermo Fisher Scientific	H3570
Chemicals, peptides, and recombinant proteins		
DMEM/F-12, GlutaMAX supplement	Thermo Fisher Scientific	10565018
fetal bovine serum	Cytiva	SH30396.03
penicillin/streptomycin	Thermo Fisher Scientific	15140122
Trypsin-EDTA (0.05%), phenol red	Thermo Fisher Scientific	25300120
PBS, pH 7.4	Thermo Fisher Scientific	10010049
Citrate Buffer, pH 6.0, 10X, Antigen Retriever	Sigma-Aldrich	C9999
Dispase II	Sigma-Aldrich	4942078001
Collagenase D	Sigma-Aldrich	11088858001
Recombinant Human Desert Hedgehog/Dhh	R&D Systems	4777-DH-050
SAG	MedChem Express	HY-12848-1mg
TRIzol	Invitrogen	15596026
Chloroform	Sigma-Aldrich	C2432
Isopropanol	Sigma-Aldrich	I9516
Poly-ethylene Glycol 8000, 50%, v/v	Rigaku	25322-68-3
Triton X-100	MilliporeSigma	T8787
RNAse Inhibitor	MilliporeSigma	3335402001
H_2O	Invitrogen	10977-015
Tris-HCl	Teknov	t5083
NaCl	Invitrogen	AM9760G

MgCl2	MilliporeSigma	M1028
GTP	Thermo Fisher Scientific	R1461
DTT	Invitrogen	P2325
dNTP	Takara	639125
Critical commercial assays		
Maxima H Minus cDNA Synthesis Master Mix	Thermo Fisher Scientific	M1661
KAPA HiFi HotStart ReadyMix	Roche	KE2502
Nextera XT DNA library Preparation Kit	Illumina	FC-131-1024
Oligonucleotides		
Smart-seq3 oligo-dT primer	Hagemann-Jensen et al.[72]	/5Biosg/ACGAGCATCAGCAGCATACGATTTTTTTTTTTTTTTTTTTTTTTTTTTTTTVN
Smart-seq3 N8 TSO	Hagemann-Jensen et al.[72]	/5Biosg/AGAGACAGATTGCGCAATGNNNNNNNNrGrGrG
Smart-seq3 Fwd primer	Hagemann-Jensen et al.[72]	TCGTCGGCAGCGTCAGATGTGTATAAGAGACAGATTGCGCAATG
Smart-seq3 Rev primer	Hagemann-Jensen et al.[72]	ACGAGCATCAGCAGCATACGA
Deposited data		
Raw sequencing data	This paper	
Processed data	This paper	
Human adipose tissue atlas	Emont et al.[41]	GEO: GSE176171
Software and algorithms		
Cell Ranger (v6.1.2)	10x Genomics	https://support.10xgenomics.com/single-cell-gene-expression/software/overview/welcome
demuxEM (v0.1.6)	Gaublomme et al.[73]	https://github.com/lilab-bcb/demuxEM
CellBender (v0.2.0)	Fleming et al.[74]	https://github.com/broadinstitute/CellBender
scDblFinder (v1.2.0)	McGinnis et al.[75]	https://github.com/plger/scDblFinder

scds (v1.4.0)	Bais et al.[76]	https://github.com/kostkalab/scds
R (v4.3.1)	R Core Team[77]	https://www.R-project.org/
Seurat (v1.4.0)	Hao et al.[78]	https://satijalab.org/seurat/
hypeR (v2.0.0)	Federico et al.[79]	https://github.com/montilab/hypeR
speckle (v1.2.0)	Phipson et al.[80]	https://github.com/phipsonlab/speckle
Slingshot (v2.10.0)	Street et al.[81]	https://bioconductor.org/packages/release/bioc/html/slingshot.html
edgeR (v4.0.16)	Robinson et al.,[82] Chen et al[83]	https://bioconductor.posit.co/packages/3.21/bioc/html/edgeR.html
rstatix (v0.7.2)	Kassambara, A.[84]	https://github.com/kassambara/rstatix/
ggplot2 (v3.5.2)	Wickham, H.[85]	https://ggplot2.tidyverse.org
arrayQualityMetrics (v3.65.0)	Kauffmann et al. [86]	https://www.bioconductor.org/packages/release/bioc/html/arrayQualityMetrics.html
Zen Black (v2.3)	Carl Zeiss Microscopy	https://www.micro-shop.zeiss.com/en/us/softwarefinder/software-categories/zen-black/zen-black-system/
FIJI ImageJ (2.14.0)	Schindelin et al.[87]	https://fiji.sc/

RESOURCE AVAILABILITY

Lead contact

Requests for further information should be directed to and will be fulfilled by the lead contact, Evan Rosen (erosen@bidmc.harvard.edu).

Data and code availability

All raw and processed sequencing data generated as part of this study will be deposited at GEO and dbGap and made publicly available at the date of publication. Accession number will be listed in the key resources table. snRNA-seq data will also be available

for viewing at the Broad Single Cell Portal (https://singlecell.broadinstitute.org/single_cell/study/SCP3587).

EXPERIMENTAL MODEL AND SUBJECT DETAILS

Subject enrollment and sample collection

Subcutaneous adipose tissue was obtained under the University of Pittsburgh Medical Center STUDY 19010309. Patients included were adults aged 21-60 undergoing bariatric surgery. Exclusion criteria were diagnosis of type 1 or type 2 diabetes, pregnancy, alcohol or drug addiction, bleeding/clotting abnormalities, or inflammatory abdominal disease. All patients provided written informed consent prior to surgery. Baseline samples were collected during bariatric surgery, and subsequent samples were obtained via a "small incisional tissue collection approach" during follow-up visits. The periumbilical skin area was anesthetized and a 6-8 mm incision was made to allow biopsy of a small piece of adipose tissue approximately 0.5-1 cc. The dermal edges were closed with sutures and a dressing was applied. The collected subcutaneous adipose tissue, approximately 0.5-1 cc (0.5 - 1 gram), was sectioned into pieces, approximately 0.25 - 0.5cc (250–500 mg), placed into cryovials, and immediately flash-frozen for subsequent processing.

Plasma profiling subject enrollment and sample collection

Fasting plasma samples were collected from patients obtaining bariatric surgery from Massachusetts General Hospital. The cohort included men and women of age >18 years who underwent Roux-en-Y gastric bypass at the time of bariatric surgery. Plasma was collected at baseline, 1-2 months and 6 months post-operatively. Patients with pre-existing cardiac disease, chronic kidney disease and uncontrolled hypertension were excluded. For this manuscript, we included results exclusively from patients who did not have diabetes and had plasma measurements recorded at all three timepoints.

Primary adipose progenitor culture

Freshly harvested mouse inguinal adipose tissues were minced and digested in a solution containing collagenase D (1.5 U/mL) and dispase II (2.4 U/mL), supplemented with 10 mM $CaCl_2$, for 15–20 minutes in a 37 °C water bath with agitation. Following digestion, wash medium (DMEM-GlutaMAX supplemented with 10% fetal bovine serum and 1% penicillin–streptomycin) was added. The digested tissue was sequentially filtered through 100 µm and 40 µm strainers, and the stromal vascular fraction (SVF) was collected and plated in growth medium (DMEM-GlutaMAX supplemented with 15% FBS and 1% penicillin–streptomycin). After 5 days of culture, adherent preadipocytes were trypsinized and replated at a density of 100,000 cells per well in collagen-coated

12-well plates. Twenty-four hours after plating, cells were treated with either the Hedgehog agonist SAG (200 nM), recombinant DHH (1 µg/mL), or the respective solvent control for 24 hours prior to RNA harvest.

Mouse VSG

C57BL/6J DIO male mice, 12-13 weeks of age, were purchased from Jackson Labs and maintained on 60% HFD (Research Diets Inc, Cat#D12492) for an additional 2-4 weeks prior to surgery. Body composition was measured using EchoMRI (Echo Medical Systems) before surgery and at the end of study. Sham and VSG surgeries were performed as described previously[34,35]. Briefly, mice were fasted overnight prior to surgery. Animals were anesthetized using isoflurane, and a small laparotomy incision was made in the abdominal wall. The lateral 80% of the stomach along the greater curvature was excised in VSG animals by using an ETS 35-mm staple gun (Ethicon Endo-Surgery). Sham surgery was performed by the application of gentle pressure on the stomach with blunt forceps for 15 seconds. All mice received one dose of Buprinex (0.1 mg/kg) and Carprofen (5 mg/kg) immediately after surgery. All mice received Carprofen (5 mg/kg) for 3 days after surgery. Animals were placed on DietGel Boost (ClearH_2O; Portland ME) for 3 days after surgery. They were placed back on the pre-operative solid diet (60% HFD) on day 4 post-surgery. Body weight and food intake as well as overall health were monitored daily for the first 7 days after surgery and once weekly until the end of the studies. Semaglutide (0.04 mg/kg) was subcutaneously administered to some Sham-operated mice once daily starting on day 5 post-surgery. Animals were sacrificed at two timepoints post-surgery, at 10 days for all groups (Timepoint 1), and at 25 days for semaglutide-treated animals and at 35 days for sham and VSG animals (Timepoint 2). All mice were sacrificed on the same calendar days with the order of sacrifice counter-balanced across all the experimental groups. Because we knew that weight loss would occur faster with Sema, we chose to dose them for 25 days to more carefully match the weight loss between the Sema and VSG-treated mice, their surgeries were performed 10 days later than the others, so that at sacrifice, all animals would be the same age. All mice were fasted for 4 hours prior to tissue collection. Terminal fasting (4 hours) glucose and insulin levels were measured at the end of the study for each cohort.

The presence of contained leaks is assessed at sacrifice in a blinded manner by three experienced surgeons. Each surgeon assigns a score to each particular sleeve and then an average score (out of three values) is calculated. Scores of 1 are assigned when the gastric sleeve is intact and similar in size to that at the time of surgery, with no adhesions present. Scores of 2-3 are assigned for a small, localized leak. Any adhesions are minor. Score 4 is assigned when the sleeve is slightly enlarged but has a single larger leak, with more moderate adhesions to the surrounding organs. Scores of

5 -7 are assigned when there is a large solitary leak to a very large leak with multiple chambers or multiple big leaks. Adhesions range from well-established to very severe. Mice with scores of 4-7 are excluded from the initial analysis primarily due to their pathomorphological changes and inflammatory profile.

METHOD DETAILS

Single-nucleus RNA sequencing and data analysis

Flash-frozen human adipose tissue samples (50-300 mg) were homogenized in gentleMACS C Tubes using a gentleMACS Tissue Dissociator with the "mr_adipose_01" program in ice-cold TST buffer, followed by sequential filtration through 40 µm and 20 µm filters. Tissue homogenates were centrifuged at 500g for 5 min at 4°C, washed in nuclei resuspension buffer (NRB), and stained with NucBlue. Individual samples were labeled with unique hashtag antibodies (TotalSeq, 2 µg/mL final concentration) through 45-minute incubation on ice, enabling multiplexing of up to 24 samples per 10X lane. Nuclei were sorted using fluorescence-activated nuclear sorting with gates for single nuclei. Sorted nuclei pools (~52,000 events targeting ~40,000 nuclei for loading) were directly loaded onto a 10X Chromium Controller following standard Single Cell 3' Gene Expression workflow with feature barcoding modifications. Endogenous cDNA and hashtag (HTO) libraries were pooled at 85:15 ratio and sequenced at ≥20,000 reads per nucleus using standard 10X read structure. Raw sequencing reads were processed with Cell Ranger using annotation GENCODE-v44, and sample demultiplexing was performed using demuxEM. Outputs were further processed with CellBender, and doublet scores were calculated using scDblFinder and scds. Cells were removed as doublets if they were both determined to be a doublet using scDblFinder and if they had a scds hybrid score > 1.5.

Count results were further analyzed with R and Seurat. Cells with <800 UMIs and with > 10% of mitochondrial reads were removed from the data object. Genes found in fewer than 2 cells were removed. The data were then normalized using SCTransform and integrated using RPCA in Seurat, integrating by individual so as not to overcorrect across timepoints. To subcluster, cells were subset into broad cell types and reintegrated and clusters were recalculated. Subclusters with high doublet scores as caculated by scDblFinder and scds were removed and subclusters were reintegrated. The final data set contains 112,991 cells with a median of 3,616 UMIs/cell and a median of 2,003 genes/cell. Reference mapping was performed between the reported dataset and the human subcutaneous dataset from Emont et. al.[41] using Seurat multimodal reference mapping. Marker genes were calculated using the Seurat Wilcoxon rank sum test with default settings. Pathway analyses were performed using the Bioconductor hypeR package. Statistical assessment of variations in cell type proportions across

different timepoints was calculated using the propeller method implemented in the speckle R package. To assess differential gene expression across post-surgical timepoints, single-cell counts were pseudobulked using Seurat's AggregateExpression function and analyzed via the edgeR Quasi-Likelihood framework. To account for the repeated-measures design, the analysis utilized an additive generalized linear model that tested for timepoint effects while using patient ID as a blocking factor. Raw p-values were adjusted using the Benjamini-Hochberg method. The trajectory of adipocyte development was built by constructing the minimum spanning tree on the Principal Component Analysis (PCA) embeddings of the ASPC subtypes and the adipocytes, using the Bioconductor Slingshot package.

SomaScan microarray data analysis

The SomaScan assay includes 5,034 SOMAmers, of which 4,783 measure human proteins from 4,137 distinct human genes A hybridization array to capture SOMAmers quantitatively determines the protein present by converting the assay signal (relative fluorescence units) into the relative abundance of an analyte. Assays were performed by SomaLogic in collaboration with Novartis.

R/Bioconductor package arrayQualityMetrics was used for microarray technical quality assessment, and data was background corrected and normalized by SomaLogic using spike in controls and calibrator samples. Differentially measured protein levels were calculated using the repeated measured ANOVA method in the rstatix R package. The p-values were adjusted using Benjamini-Hochberg method to control for the false discovery rate (FDR). Proteins were considered significantly changed if they had an FDR-adjusted p value <0.05 and a fold change greater than 20%.

For the analysis in this manuscript, we used a subset of the original dataset, including only profiles from non-diabetic donors. Furthermore, we restricted the data to only those profiles with complete measurements across all three time points (n=35).

Immunofluorescence and blood vessel quantification

Flash-frozen adipose tissue biopsies were partially thawed from -80°C to -20°C for 24 hours, then fixated in 10% formalin overnight at 4°C under constant rotation. Fixation was followed by paraffin embedding, sectioning, and staining with hematoxylin and eosin (H&E) to assess section quality. Unstained sections for immunofluorescence were deparaffinized and rehydrated by heating to 55°C and sequential washing in xylene, 100%, 95%, 70%, 50% ethanol and deionized water. Antigen retrieval was performed in sub-boiling 10 mM sodium citrate buffer for 10 min. Sections were washed with 1% donkey serum in PBS with 0.4% Triton X-100 (PBS-T) twice, and blocked with 5% donkey serum in PBS-T for 30 minutes. Sections were then incubated with the primary

antibodies diluted in 1% donkey serum PBS-T at room temperature for 1 h and then at 4°C overnight. Primary antibodies and dilutions used for labeling were: Alexa Fluor 488 mouse anti-CD31 (1:100) and rabbit anti-DHH (1:100). Samples were subsequently incubated with secondary antibody Alexa Fluor 647 donkey anti-rabbit (1:250) and Hoechst 33342 (1:1000) diluted in PBS-T at room temperature for 1 hour. Images were obtained using a Zeiss LSM 880 laser scanning confocal system running Zen Black software. Images were analyzed using ImageJ Fiji software. To quantify DHH^+ blood vessels, tissue sections were fluorescently immunolabeled for CD31 and DHH as above. Five equally powered fields per sample were evaluated for quantification. DHH^+CD31^+ double-positive vessel segments were quantified as a percentage of total $CD31^+$ vessel segments.

RNA isolation for bulk RNA-sequencing

Cells in culture wells were collected with TRIzol reagent. The cell-TRIzol mixtures were transferred to collection tubes and homogenized with a Tissuelyser II (QIAGEN). Chloroform was added in a 1:5 ratio by volume and phase separation was performed. The RNA-containing layer was transferred to new tubes, mixed with an equal volume of 100% isopropanol and incubated overnight at −80 °C for precipitation. Precipitated RNA was with 80% ethanol and resuspended in nuclease-free water. RNA concentration and purity were determined using a NanoDrop 2000 (Thermo Scientific). RNA was sent for bulk RNA-sequencing by the Boston Area Diabetes Endocrinology Research Center (BADERC) Functional Genomics Core.

Bulk RNA-sequencing and data analysis

Bulk RNA-sequencing data was generated following the Smart-seq3 protocol described by Hagemann-Jensen, M.[72] Samples were reverse transcribed and template switched using the Maxima H Minus cDNA Synthesis Master Mix and the cDNA were subsequently amplified using Kapa HiFi HotStart ReadyMix. Library construction was performed with the Nextera XT DNA Library Preparation Kit. Differential expressions between treatments and controls were evaluated with the Wald test implemented in the DESeq2 R package. Enrichment analysis was performed using the Bioconductor hypeR package.

REFERENCES

1. Barrett TS, Hafermann JO, Richards S, LeJeune K, Eid GM. Obesity Treatment With Bariatric Surgery vs GLP-1 Receptor Agonists. *JAMA Surg*. Nov 1 2025;160(11):1232-1239. doi:10.1001/jamasurg.2025.3590
2. Loft A, Emont MP, Weinstock A, et al. Towards a consensus atlas of human and mouse adipose tissue at single-cell resolution. *Nat Metab*. May 2025;7(5):875-894. doi:10.1038/s42255-025-01296-9
3. Maniyadath B, Zhang Q, Gupta RK, Mandrup S. Adipose tissue at single-cell resolution. *Cell Metab*. Mar 7 2023;35(3):386-413. doi:10.1016/j.cmet.2023.02.002
4. Weisberg SP, McCann D, Desai M, Rosenbaum M, Leibel RL, Ferrante AW, Jr. Obesity is associated with macrophage accumulation in adipose tissue. *J Clin Invest*. Dec 2003;112(12):1796-808. doi:10.1172/JCI19246
5. Kawai T, Autieri MV, Scalia R. Adipose tissue inflammation and metabolic dysfunction in obesity. *Am J Physiol Cell Physiol*. Mar 1 2021;320(3):C375-C391. doi:10.1152/ajpcell.00379.2020
6. Guilherme A, Virbasius JV, Puri V, Czech MP. Adipocyte dysfunctions linking obesity to insulin resistance and type 2 diabetes. *Nat Rev Mol Cell Biol*. May 2008;9(5):367-77. doi:10.1038/nrm2391
7. Goossens GH, Blaak EE. Adipose tissue dysfunction and impaired metabolic health in human obesity: a matter of oxygen? *Front Endocrinol (Lausanne)*. 2015;6:55. doi:10.3389/fendo.2015.00055
8. Hinte LC, Castellano-Castillo D, Ghosh A, et al. Adipose tissue retains an epigenetic memory of obesity after weight loss. *Nature*. Dec 2024;636(8042):457-465. doi:10.1038/s41586-024-08165-7
9. Miranda AMA, McAllan L, Mazzei G, et al. Selective remodelling of the adipose niche in obesity and weight loss. *Nature*. Aug 2025;644(8077):769-779. doi:10.1038/s41586-025-09233-2
10. Loft A, Rydbirk R, Klinggaard EG, et al. Single-cell-resolved transcriptional dynamics of human subcutaneous adipose tissue during lifestyle- and bariatric surgery-induced weight loss. *Nat Metab*. Jan 12 2026;doi:10.1038/s42255-025-01433-4
11. Salans LB, Horton ES, Sims EA. Experimental obesity in man: cellular character of the adipose tissue. *J Clin Invest*. May 1971;50(5):1005-11. doi:10.1172/JCI106570
12. Spalding KL, Arner E, Westermark PO, et al. Dynamics of fat cell turnover in humans. *Nature*. Jun 5 2008;453(7196):783-7. doi:10.1038/nature06902
13. Corey KE, Pitts R, Lai M, et al. ADAMTSL2 protein and a soluble biomarker signature identify at-risk non-alcoholic steatohepatitis and fibrosis in adults with NAFLD. *J Hepatol*. Jan 2022;76(1):25-33. doi:10.1016/j.jhep.2021.09.026
14. Jaitin DA, Adlung L, Thaiss CA, et al. Lipid-Associated Macrophages Control Metabolic Homeostasis in a Trem2-Dependent Manner. *Cell*. Jul 25 2019;178(3):686-698 e14. doi:10.1016/j.cell.2019.05.054
15. Cinti S, Mitchell G, Barbatelli G, et al. Adipocyte death defines macrophage localization and function in adipose tissue of obese mice and humans. *J Lipid Res*. Nov 2005;46(11):2347-55. doi:10.1194/jlr.M500294-JLR200

16. Merrick D, Sakers A, Irgebay Z, et al. Identification of a mesenchymal progenitor cell hierarchy in adipose tissue. *Science*. Apr 26 2019;364(6438)doi:10.1126/science.aav2501
17. Schwalie PC, Dong H, Zachara M, et al. A stromal cell population that inhibits adipogenesis in mammalian fat depots. *Nature*. Jul 2018;559(7712):103-108. doi:10.1038/s41586-018-0226-8
18. Pratap J, Galindo M, Zaidi SK, et al. Cell growth regulatory role of Runx2 during proliferative expansion of preosteoblasts. *Cancer Res*. Sep 1 2003;63(17):5357-62.
19. Kim W, Barron DA, San Martin R, et al. RUNX1 is essential for mesenchymal stem cell proliferation and myofibroblast differentiation. *Proc Natl Acad Sci U S A*. Nov 18 2014;111(46):16389-94. doi:10.1073/pnas.1407097111
20. VanOudenhove JJ, Medina R, Ghule PN, et al. Transient RUNX1 Expression during Early Mesendodermal Differentiation of hESCs Promotes Epithelial to Mesenchymal Transition through TGFB2 Signaling. *Stem Cell Reports*. Nov 8 2016;7(5):884-896. doi:10.1016/j.stemcr.2016.09.006
21. Cao Z, Umek RM, McKnight SL. Regulated expression of three C/EBP isoforms during adipose conversion of 3T3-L1 cells. *Genes Dev*. Sep 1991;5(9):1538-52. doi:10.1101/gad.5.9.1538
22. Tontonoz P, Hu E, Spiegelman BM. Stimulation of adipogenesis in fibroblasts by PPAR gamma 2, a lipid-activated transcription factor. *Cell*. Dec 30 1994;79(7):1147-56. doi:10.1016/0092-8674(94)90006-x
23. Lin FT, Lane MD. CCAAT/enhancer binding protein alpha is sufficient to initiate the 3T3-L1 adipocyte differentiation program. *Proc Natl Acad Sci U S A*. Sep 13 1994;91(19):8757-61. doi:10.1073/pnas.91.19.8757
24. Laufer E, Nelson CE, Johnson RL, Morgan BA, Tabin C. Sonic hedgehog and Fgf-4 act through a signaling cascade and feedback loop to integrate growth and patterning of the developing limb bud. *Cell*. Dec 16 1994;79(6):993-1003. doi:10.1016/0092-8674(94)90030-2
25. Porter JA, Ekker SC, Park WJ, et al. Hedgehog patterning activity: role of a lipophilic modification mediated by the carboxy-terminal autoprocessing domain. *Cell*. Jul 12 1996;86(1):21-34. doi:10.1016/s0092-8674(00)80074-4
26. Suh JM, Gao X, McKay J, McKay R, Salo Z, Graff JM. Hedgehog signaling plays a conserved role in inhibiting fat formation. *Cell Metab*. Jan 2006;3(1):25-34. doi:10.1016/j.cmet.2005.11.012
27. Kopinke D, Roberson EC, Reiter JF. Ciliary Hedgehog Signaling Restricts Injury-Induced Adipogenesis. *Cell*. Jul 13 2017;170(2):340-351 e12. doi:10.1016/j.cell.2017.06.035
28. Isakson P, Hammarstedt A, Gustafson B, Smith U. Impaired preadipocyte differentiation in human abdominal obesity: role of Wnt, tumor necrosis factor-alpha, and inflammation. *Diabetes*. Jul 2009;58(7):1550-7. doi:10.2337/db08-1770
29. Palmer AK, Xu M, Zhu Y, et al. Targeting senescent cells alleviates obesity-induced metabolic dysfunction. *Aging Cell*. Jun 2019;18(3):e12950. doi:10.1111/acel.12950
30. Rouault C, Marcelin G, Adriouch S, et al. Senescence-associated beta-galactosidase in subcutaneous adipose tissue associates with altered glycaemic status and truncal fat in severe obesity. *Diabetologia*. Jan 2021;64(1):240-254. doi:10.1007/s00125-020-05307-0

31. Regulski MJ. Cellular Senescence: What, Why, and How. *Wounds*. Jun 2017;29(6):168-174.
32. Suresh S, Karthik G, Ouyang JF, et al. SenMayo transcriptomic senescence panel highlights glial cells in the ageing mouse and human retina. *NPJ Aging*. Nov 30 2024;10(1):60. doi:10.1038/s41514-024-00187-9
33. Ragueneau E, Gong C, Sinquin P, et al. The Reactome Knowledgebase 2026. *Nucleic Acids Res*. Jan 6 2026;54(D1):D673-D681. doi:10.1093/nar/gkaf1223
34. Emont MP, Essene AL, Gulko A, et al. Semaglutide and bariatric surgery induce distinct changes in the composition of mouse white adipose tissue. *Mol Metab*. May 2025;95:102126. doi:10.1016/j.molmet.2025.102126
35. Hao Z, Townsend RL, Mumphrey MB, Morrison CD, Munzberg H, Berthoud HR. RYGB Produces more Sustained Body Weight Loss and Improvement of Glycemic Control Compared with VSG in the Diet-Induced Obese Mouse Model. *Obes Surg*. Sep 2017;27(9):2424-2433. doi:10.1007/s11695-017-2660-3
36. Lee CH, Lam KS. Obesity-induced insulin resistance and macrophage infiltration of the adipose tissue: A vicious cycle. *J Diabetes Investig*. Jan 2019;10(1):29-31. doi:10.1111/jdi.12918
37. Trayhurn P. Hypoxia and adipose tissue function and dysfunction in obesity. *Physiol Rev*. Jan 2013;93(1):1-21. doi:10.1152/physrev.00017.2012
38. Cao Y. Angiogenesis modulates adipogenesis and obesity. *J Clin Invest*. Sep 2007;117(9):2362-8. doi:10.1172/JCI32239
39. Sun K, Kusminski CM, Scherer PE. Adipose tissue remodeling and obesity. *J Clin Invest*. Jun 2011;121(6):2094-101. doi:10.1172/JCI45887
40. Raulerson CK, Ko A, Kidd JC, et al. Adipose Tissue Gene Expression Associations Reveal Hundreds of Candidate Genes for Cardiometabolic Traits. *Am J Hum Genet*. Oct 3 2019;105(4):773-787. doi:10.1016/j.ajhg.2019.09.001
41. Emont MP, Jacobs C, Essene AL, et al. A single-cell atlas of human and mouse white adipose tissue. *Nature*. Mar 2022;603(7903):926-933. doi:10.1038/s41586-022-04518-2
42. Lemoine AY, Ledoux S, Queguiner I, et al. Link between adipose tissue angiogenesis and fat accumulation in severely obese subjects. *J Clin Endocrinol Metab*. May 2012;97(5):E775-80. doi:10.1210/jc.2011-2649
43. Lee YS, Kim JW, Osborne O, et al. Increased adipocyte O2 consumption triggers HIF-1alpha, causing inflammation and insulin resistance in obesity. *Cell*. Jun 5 2014;157(6):1339-1352. doi:10.1016/j.cell.2014.05.012
44. Yan S, Santoro A, Niphakis MJ, et al. Inflammation causes insulin resistance in mice via interferon regulatory factor 3 (IRF3)-mediated reduction in FAHFA levels. *Nat Commun*. May 30 2024;15(1):4605. doi:10.1038/s41467-024-48220-5
45. Li Q, Hagberg CE, Silva Cascales H, et al. Obesity and hyperinsulinemia drive adipocytes to activate a cell cycle program and senesce. *Nat Med*. Nov 2021;27(11):1941-1953. doi:10.1038/s41591-021-01501-8
46. Zhang Y, Huang C. Targeting adipocyte apoptosis: a novel strategy for obesity therapy. *Biochem Biophys Res Commun*. Jan 6 2012;417(1):1-4. doi:10.1016/j.bbrc.2011.11.158

47. Alkhouri N, Gornicka A, Berk MP, et al. Adipocyte apoptosis, a link between obesity, insulin resistance, and hepatic steatosis. *J Biol Chem*. Jan 29 2010;285(5):3428-38. doi:10.1074/jbc.M109.074252
48. Luk CT, Chan CK, Chiu F, et al. Dual Role of Caspase 8 in Adipocyte Apoptosis and Metabolic Inflammation. *Diabetes*. Dec 1 2023;72(12):1751-1765. doi:10.2337/db22-1033
49. Wilson CH, Nikolic A, Kentish SJ, et al. Caspase-2 deficiency enhances whole-body carbohydrate utilisation and prevents high-fat diet-induced obesity. *Cell Death Dis*. Oct 26 2017;8(10):e3136. doi:10.1038/cddis.2017.518
50. Machado MV, Michelotti GA, Jewell ML, et al. Caspase-2 promotes obesity, the metabolic syndrome and nonalcoholic fatty liver disease. *Cell Death Dis*. Feb 18 2016;7(2):e2096. doi:10.1038/cddis.2016.19
51. Chin HS, Li MX, Tan IKL, et al. VDAC2 enables BAX to mediate apoptosis and limit tumor development. *Nat Commun*. Nov 26 2018;9(1):4976. doi:10.1038/s41467-018-07309-4
52. Yuan Z, Dewson G, Czabotar PE, Birkinshaw RW. VDAC2 and the BCL-2 family of proteins. *Biochem Soc Trans*. Dec 17 2021;49(6):2787-2795. doi:10.1042/BST20210753
53. Sun F, Li X, Duan WQ, et al. Transforming Growth Factor-beta Receptor III is a Potential Regulator of Ischemia-Induced Cardiomyocyte Apoptosis. *J Am Heart Assoc*. May 30 2017;6(6)doi:10.1161/JAHA.116.005357
54. Solito E, Kamal A, Russo-Marie F, Buckingham JC, Marullo S, Perretti M. A novel calcium-dependent proapoptotic effect of annexin 1 on human neutrophils. *FASEB J*. Aug 2003;17(11):1544-6. doi:10.1096/fj.02-0941fje
55. Levy-Strumpf N, Kimchi A. Death associated proteins (DAPs): from gene identification to the analysis of their apoptotic and tumor suppressive functions. *Oncogene*. Dec 24 1998;17(25):3331-40. doi:10.1038/sj.onc.1202588
56. Gao J, Senthil M, Ren B, et al. IRF-1 transcriptionally upregulates PUMA, which mediates the mitochondrial apoptotic pathway in IRF-1-induced apoptosis in cancer cells. *Cell Death Differ*. Apr 2010;17(4):699-709. doi:10.1038/cdd.2009.156
57. Gurr MI, Jung RT, Robinson MP, James WP. Adipose tissue cellularity in man: the relationship between fat cell size and number, the mass and distribution of body fat and the history of weight gain and loss. *Int J Obes*. 1982;6(5):419-36.
58. MacLean PS, Higgins JA, Jackman MR, et al. Peripheral metabolic responses to prolonged weight reduction that promote rapid, efficient regain in obesity-prone rats. *Am J Physiol Regul Integr Comp Physiol*. Jun 2006;290(6):R1577-88. doi:10.1152/ajpregu.00810.2005
59. Miller WH, Jr., Faust IM, Goldberger AC, Hirsch J. Effects of severe long-term food deprivation and refeeding on adipose tissue cells in the rat. *Am J Physiol*. Jul 1983;245(1):E74-80. doi:10.1152/ajpendo.1983.245.1.E74
60. Gustafson B, Smith U. The WNT inhibitor Dickkopf 1 and bone morphogenetic protein 4 rescue adipogenesis in hypertrophic obesity in humans. *Diabetes*. May 2012;61(5):1217-24. doi:10.2337/db11-1419
61. Gustafson B, Hammarstedt A, Hedjazifar S, Smith U. Restricted adipogenesis in hypertrophic obesity: the role of WISP2, WNT, and BMP4. *Diabetes*. Sep 2013;62(9):2997-3004. doi:10.2337/db13-0473

62. Arner E, Westermark PO, Spalding KL, et al. Adipocyte turnover: relevance to human adipose tissue morphology. *Diabetes*. Jan 2010;59(1):105-9. doi:10.2337/db09-0942
63. Rossmeislova L, Malisova L, Kracmerova J, et al. Weight loss improves the adipogenic capacity of human preadipocytes and modulates their secretory profile. *Diabetes*. Jun 2013;62(6):1990-5. doi:10.2337/db12-0986
64. Pospisilik JA, Schramek D, Schnidar H, et al. Drosophila genome-wide obesity screen reveals hedgehog as a determinant of brown versus white adipose cell fate. *Cell*. Jan 8 2010;140(1):148-60. doi:10.1016/j.cell.2009.12.027
65. Fontaine C, Cousin W, Plaisant M, Dani C, Peraldi P. Hedgehog signaling alters adipocyte maturation of human mesenchymal stem cells. *Stem Cells*. Apr 2008;26(4):1037-46. doi:10.1634/stemcells.2007-0974
66. Kong W, Lu WJ, Dubey M, et al. Neuroendocrine cells orchestrate regeneration through Desert hedgehog signaling. *Cell*. Sep 4 2025;188(18):5020-5038 e20. doi:10.1016/j.cell.2025.05.012
67. Pola R, Ling LE, Silver M, et al. The morphogen Sonic hedgehog is an indirect angiogenic agent upregulating two families of angiogenic growth factors. *Nat Med*. Jun 2001;7(6):706-11. doi:10.1038/89083
68. Byrd N, Becker S, Maye P, et al. Hedgehog is required for murine yolk sac angiogenesis. *Development*. Jan 2002;129(2):361-72. doi:10.1242/dev.129.2.361
69. Williams C, Kim SH, Ni TT, et al. Hedgehog signaling induces arterial endothelial cell formation by repressing venous cell fate. *Dev Biol*. May 1 2010;341(1):196-204. doi:10.1016/j.ydbio.2010.02.028
70. Porter JA, von Kessler DP, Ekker SC, et al. The product of hedgehog autoproteolytic cleavage active in local and long-range signalling. *Nature*. Mar 23 1995;374(6520):363-6. doi:10.1038/374363a0
71. Porter JA, Young KE, Beachy PA. Cholesterol modification of hedgehog signaling proteins in animal development. *Science*. Oct 11 1996;274(5285):255-9. doi:10.1126/science.274.5285.255
72. Hagemann-Jensen M, Ziegenhain C, Chen P, et al. Single-cell RNA counting at allele and isoform resolution using Smart-seq3. *Nat Biotechnol*. Jun 2020;38(6):708-714. doi:10.1038/s41587-020-0497-0
73. Gaublomme JT, Li B, McCabe C, et al. Nuclei multiplexing with barcoded antibodies for single-nucleus genomics. *Nat Commun*. Jul 2 2019;10(1):2907. doi:10.1038/s41467-019-10756-2
74. Fleming SJ, Chaffin MD, Arduini A, et al. Unsupervised removal of systematic background noise from droplet-based single-cell experiments using CellBender. *Nat Methods*. Sep 2023;20(9):1323-1335. doi:10.1038/s41592-023-01943-7
75. McGinnis CS, Murrow LM, Gartner ZJ. DoubletFinder: Doublet Detection in Single-Cell RNA Sequencing Data Using Artificial Nearest Neighbors. *Cell Syst*. Apr 24 2019;8(4):329-337 e4. doi:10.1016/j.cels.2019.03.003
76. Bais AS, Kostka D. scds: computational annotation of doublets in single-cell RNA sequencing data. *Bioinformatics*. Feb 15 2020;36(4):1150-1158. doi:10.1093/bioinformatics/btz698
77. R Core Team. R: A Language and Environment for Statistical Computing. 2023.

78. Hao Y, Hao S, Andersen-Nissen E, et al. Integrated analysis of multimodal single-cell data. *Cell*. Jun 24 2021;184(13):3573-3587 e29. doi:10.1016/j.cell.2021.04.048
79. Federico A, Monti S. hypeR: an R package for geneset enrichment workflows. *Bioinformatics*. Feb 15 2020;36(4):1307-1308. doi:10.1093/bioinformatics/btz700
80. Phipson B, Sim CB, Porrello ER, Hewitt AW, Powell J, Oshlack A. propeller: testing for differences in cell type proportions in single cell data. *Bioinformatics*. Oct 14 2022;38(20):4720-4726. doi:10.1093/bioinformatics/btac582
81. Street K, Risso D, Fletcher RB, et al. Slingshot: cell lineage and pseudotime inference for single-cell transcriptomics. *BMC Genomics*. Jun 19 2018;19(1):477. doi:10.1186/s12864-018-4772-0
82. Robinson MD, McCarthy DJ, Smyth GK. edgeR: a Bioconductor package for differential expression analysis of digital gene expression data. *Bioinformatics*. Jan 1 2010;26(1):139-40. doi:10.1093/bioinformatics/btp616
83. Chen Y, Chen L, Lun ATL, Baldoni PL, Smyth GK. edgeR v4: powerful differential analysis of sequencing data with expanded functionality and improved support for small counts and larger datasets. *Nucleic Acids Res*. Jan 11 2025;53(2)doi:10.1093/nar/gkaf018
84. Kassambara A. rstatix: Pipe-Friendly Framework for Basic Statistical Tests. 2023.
85. Wickham H. *ggplot2: Elegant Graphics for Data Analysis*. Springer-Verlag New York; 2016.
86. Kauffmann A, Gentleman R, Huber W. arrayQualityMetrics--a bioconductor package for quality assessment of microarray data. *Bioinformatics*. Feb 1 2009;25(3):415-6. doi:10.1093/bioinformatics/btn647
87. Schindelin J, Arganda-Carreras I, Frise E, et al. Fiji: an open-source platform for biological-image analysis. *Nat Methods*. Jun 28 2012;9(7):676-82. doi:10.1038/nmeth.2019

Figure 1

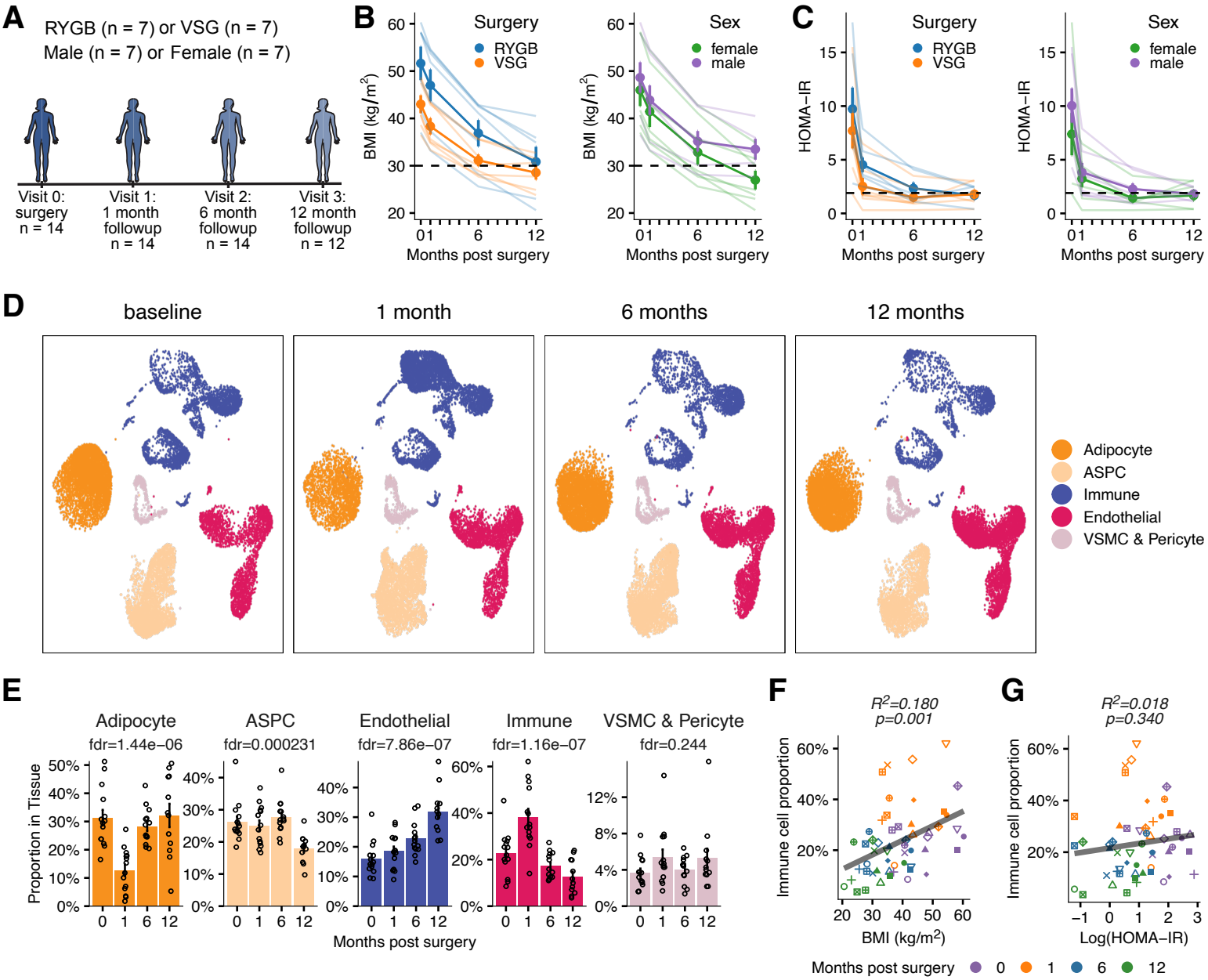
A
RYGB (n = 7) or VSG (n = 7)
Male (n = 7) or Female (n = 7)
Visit 0: surgery n = 14
Visit 1: 1 month followup n = 14
Visit 2: 6 month followup n = 14
Visit 3: 12 month followup n = 12
B
Surgery
RYGB
VSG
Sex
female
male
BMI (kg/m2)
Months post surgery
C
HOMA−IR
Months post surgery
D
baseline
1 month
6 months
12 months
Adipocyte
ASPC
Immune
Endothelial
VSMC & Pericyte
E
Adipocyte
fdr=1.44e−06
ASPC
fdr=0.000231
Endothelial
fdr=7.86e−07
Immune
fdr=1.16e−07
VSMC & Pericyte
fdr=0.244
Proportion in Tissue
Months post surgery
F
R2=0.180
p=0.001
Immune cell proportion
BMI (kg/m2)
G
R2=0.018
p=0.340
Log(HOMA−IR)
Months post surgery

Figure 2

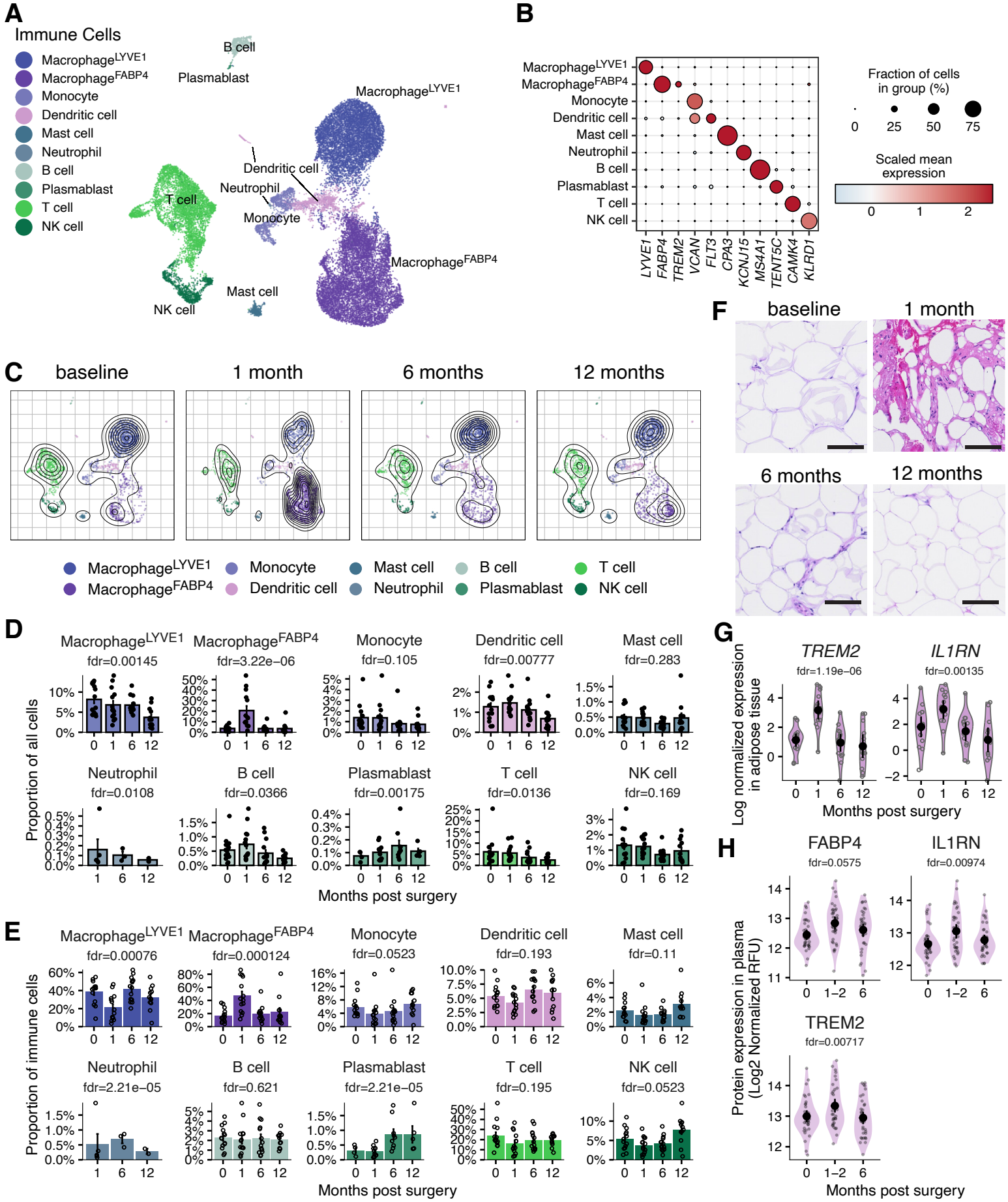
A
Immune Cells
Macrophage LYVE1
Macrophage FABP4
Monocyte
Dendritic cell
Mast cell
Neutrophil
B cell
Plasmablast
T cell
NK cell
B cell
Plasmablast
Macrophage LYVE1
Dendritic cell
Neutrophil
T cell
Monocyte
Macrophage FABP4
Mast cell
NK cell
B
Fraction of cells in group (%)
0 25 50 75
Scaled mean expression
0 1 2
LYVE1 FABP4 TREM2 VCAN FLT3 CPA3 KCNJ15 MS4A1 TENT5C CAMK4 KLRD1
C
baseline
1 month
6 months
12 months
D
Proportion of all cells
Macrophage LYVE1 fdr=0.00145
Macrophage FABP4 fdr=3.22e−06
Monocyte fdr=0.105
Dendritic cell fdr=0.00777
Mast cell fdr=0.283
Neutrophil fdr=0.0108
B cell fdr=0.0366
Plasmablast fdr=0.00175
T cell fdr=0.0136
NK cell fdr=0.169
Months post surgery
E
Proportion of immune cells
Macrophage LYVE1 fdr=0.00076
Macrophage FABP4 fdr=0.000124
Monocyte fdr=0.0523
Dendritic cell fdr=0.193
Mast cell fdr=0.11
Neutrophil fdr=2.21e−05
B cell fdr=0.621
Plasmablast fdr=2.21e−05
T cell fdr=0.195
NK cell fdr=0.0523
Months post surgery
F
baseline
1 month
6 months
12 months
G
Log normalized expression in adipose tissue
TREM2 fdr=1.19e−06
IL1RN fdr=0.00135
Months post surgery
H
Protein expression in plasma (Log2 Normalized RFU)
FABP4 fdr=0.0575
IL1RN fdr=0.00974
TREM2 fdr=0.00717
Months post surgery

Figure 3

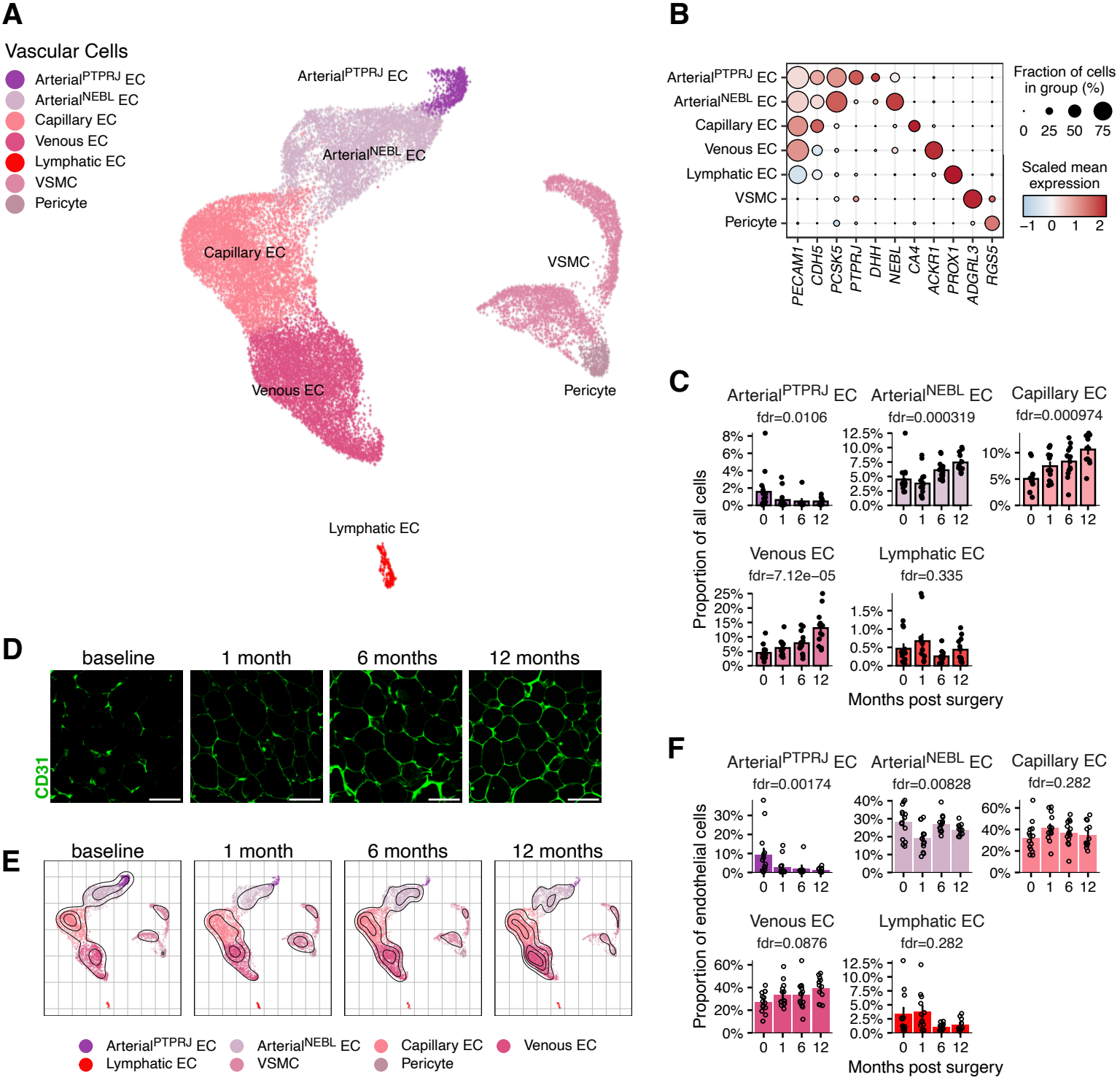
A
Vascular Cells
Arterial^PTPRJ EC
Arterial^NEBL EC
Capillary EC
Venous EC
Lymphatic EC
VSMC
Pericyte
B
Fraction of cells in group (%)
0 25 50 75
Scaled mean expression
−1 0 1 2
PECAM1 CDH5 PCSK5 PTPRJ DHH NEBL CA4 ACKR1 PROX1 ADGRL3 RGS5
C
fdr=0.0106
fdr=0.000319
fdr=0.000974
fdr=7.12e−05
fdr=0.335
Proportion of all cells
Months post surgery
D
baseline
1 month
6 months
12 months
CD31
E
F
fdr=0.00174
fdr=0.00828
fdr=0.282
fdr=0.0876
fdr=0.282
Proportion of endothelial cells
Months post surgery

Figure 4

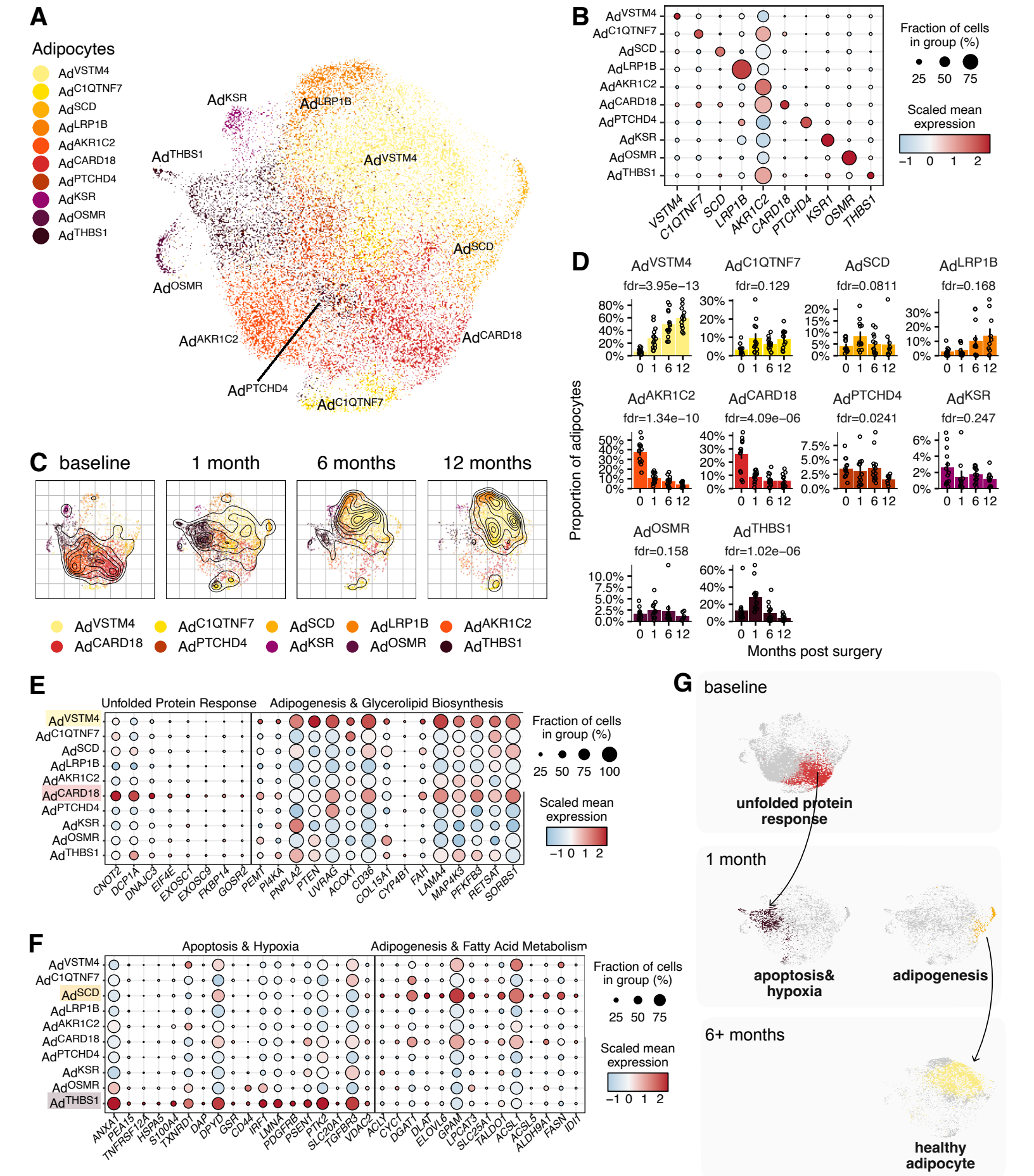
A
Adipocytes
Ad^VSTM4
Ad^C1QTNF7
Ad^SCD
Ad^LRP1B
Ad^AKR1C2
Ad^CARD18
Ad^PTCHD4
Ad^KSR
Ad^OSMR
Ad^THBS1
B
Fraction of cells in group (%)
25 50 75
Scaled mean expression
−1 0 1 2
VSTM4 C1QTNF7 SCD LRP1B AKR1C2 CARD18 PTCHD4 KSR1 OSMR THBS1
C
baseline
1 month
6 months
12 months
D
fdr=3.95e−13
fdr=0.129
fdr=0.0811
fdr=0.168
fdr=1.34e−10
fdr=4.09e−06
fdr=0.0241
fdr=0.247
fdr=0.158
fdr=1.02e−06
Proportion of adipocytes
Months post surgery
E
Unfolded Protein Response
Adipogenesis & Glycerolipid Biosynthesis
CNOT2 DCP1A DNAJC3 EIF4E EXOSC1 EXOSC9 FKBP14 GOSR2 PEMT PI4KA PNPLA2 PTEN UVRAG ACOX1 CD36 COL15A1 CYP4B1 FAH LAMA4 MAP4K3 PFKFB3 RETSAT SORBS1
F
Apoptosis & Hypoxia
Adipogenesis & Fatty Acid Metabolism
ANXA1 PEA15 TNFRSF12A HSPA5 S100A4 TXNRD1 DAP DPYD GSR CD44 IRF1 LMNA PDGFRB PSEN1 PTK2 SLC20A1 TGFBR3 VDAC2 ACLY CYC1 DGAT1 DLAT ELOVL6 GPAM LPCAT3 SLC25A1 TALDO1 ACSL1 ACSL5 ALDH9A1 FASN IDH1
G
baseline
unfolded protein response
1 month
apoptosis& hypoxia
adipogenesis
6+ months
healthy adipocyte

Figure 5

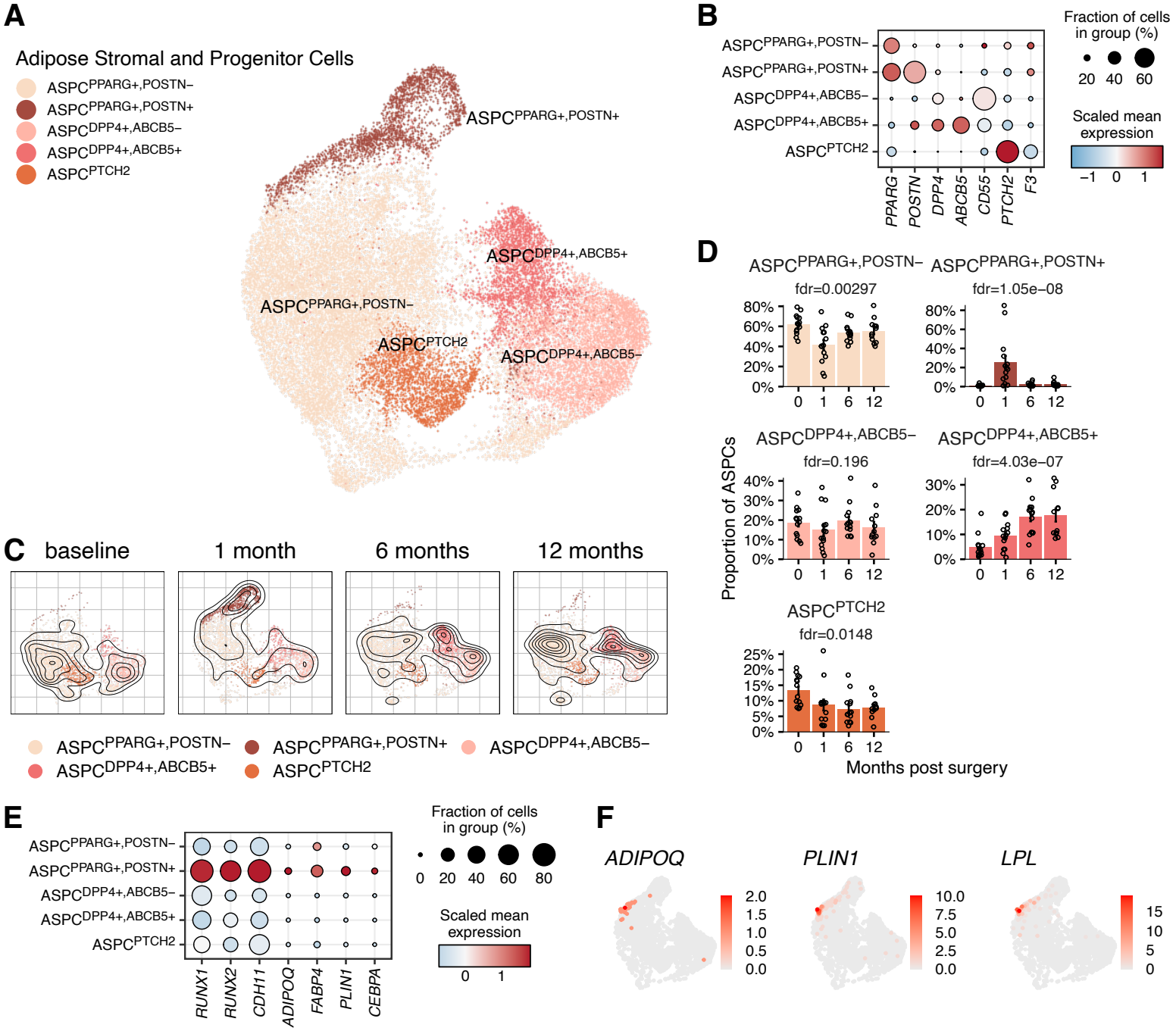
A
Adipose Stromal and Progenitor Cells
ASPC^PPARG+,POSTN−
ASPC^PPARG+,POSTN+
ASPC^DPP4+,ABCB5−
ASPC^DPP4+,ABCB5+
ASPC^PTCH2
B
Fraction of cells in group (%)
20 40 60
Scaled mean expression
−1 0 1
PPARG POSTN DPP4 ABCB5 CD55 PTCH2 F3
C
baseline
1 month
6 months
12 months
D
fdr=0.00297
fdr=1.05e−08
fdr=0.196
fdr=4.03e−07
fdr=0.0148
Proportion of ASPCs
Months post surgery
E
Fraction of cells in group (%)
0 20 40 60 80
Scaled mean expression
0 1
RUNX1 RUNX2 CDH11 ADIPOQ FABP4 PLIN1 CEBPA
F
ADIPOQ
PLIN1
LPL

Figure 6

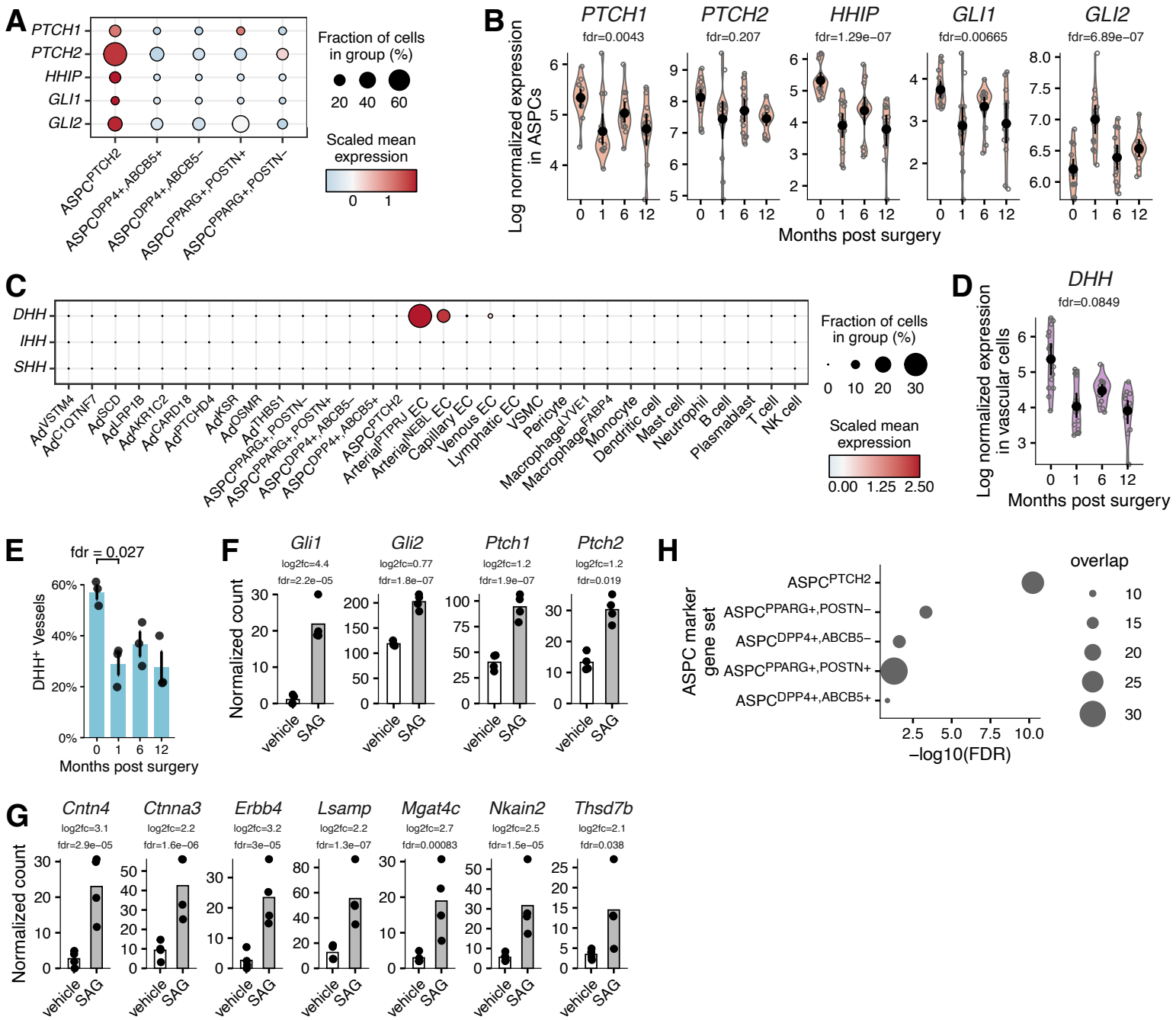
A
PTCH1
PTCH2
HHIP
GLI1
GLI2
ASPC^PTCH2
ASPC^DPP4+,ABCB5+
ASPC^DPP4+,ABCB5−
ASPC^PPARG+,POSTN+
ASPC^PPARG+,POSTN−
Fraction of cells in group (%)
20 40 60
Scaled mean expression
0 1
B
PTCH1
fdr=0.0043
PTCH2
fdr=0.207
HHIP
fdr=1.29e−07
GLI1
fdr=0.00665
GLI2
fdr=6.89e−07
Log normalized expression in ASPCs
Months post surgery
C
DHH
IHH
SHH
AdVSTM4
AdC1QTNF7
AdSCD
AdLRP1B
AdAKR1C2
AdCARD18
AdPTCHD4
AdKSR
AdOSMR
AdTHBS1
ASPC^PPARG+,POSTN−
ASPC^PPARG+,POSTN+
ASPC^DPP4+,ABCB5−
ASPC^DPP4+,ABCB5+
ASPC^PTCH2
Arterial^PTPRJ EC
Arterial^NEBL EC
Capillary EC
Venous EC
Lymphatic EC
VSMC
Pericyte
Macrophage^LYVE1
Macrophage^FABP4
Monocyte
Dendritic cell
Mast cell
Neutrophil
B cell
Plasmablast
T cell
NK cell
Fraction of cells in group (%)
0 10 20 30
Scaled mean expression
0.00 1.25 2.50
D
DHH
fdr=0.0849
Log normalized expression in vascular cells
Months post surgery
E
fdr = 0.027
DHH+ Vessels
Months post surgery
F
Gli1
log2fc=4.4
fdr=2.2e−05
Gli2
log2fc=0.77
fdr=1.8e−07
Ptch1
log2fc=1.2
fdr=1.9e−07
Ptch2
log2fc=1.2
fdr=0.019
Normalized count
vehicle
SAG
H
ASPC marker gene set
ASPC^PTCH2
ASPC^PPARG+,POSTN−
ASPC^DPP4+,ABCB5−
ASPC^PPARG+,POSTN+
ASPC^DPP4+,ABCB5+
−log10(FDR)
overlap
G
Cntn4
log2fc=3.1
fdr=2.9e−05
Ctnna3
log2fc=2.2
fdr=1.6e−06
Erbb4
log2fc=3.2
fdr=3e−05
Lsamp
log2fc=2.2
fdr=1.3e−07
Mgat4c
log2fc=2.7
fdr=0.00083
Nkain2
log2fc=2.5
fdr=1.5e−05
Thsd7b
log2fc=2.1
fdr=0.038
Normalized count
vehicle
SAG

Figure 7

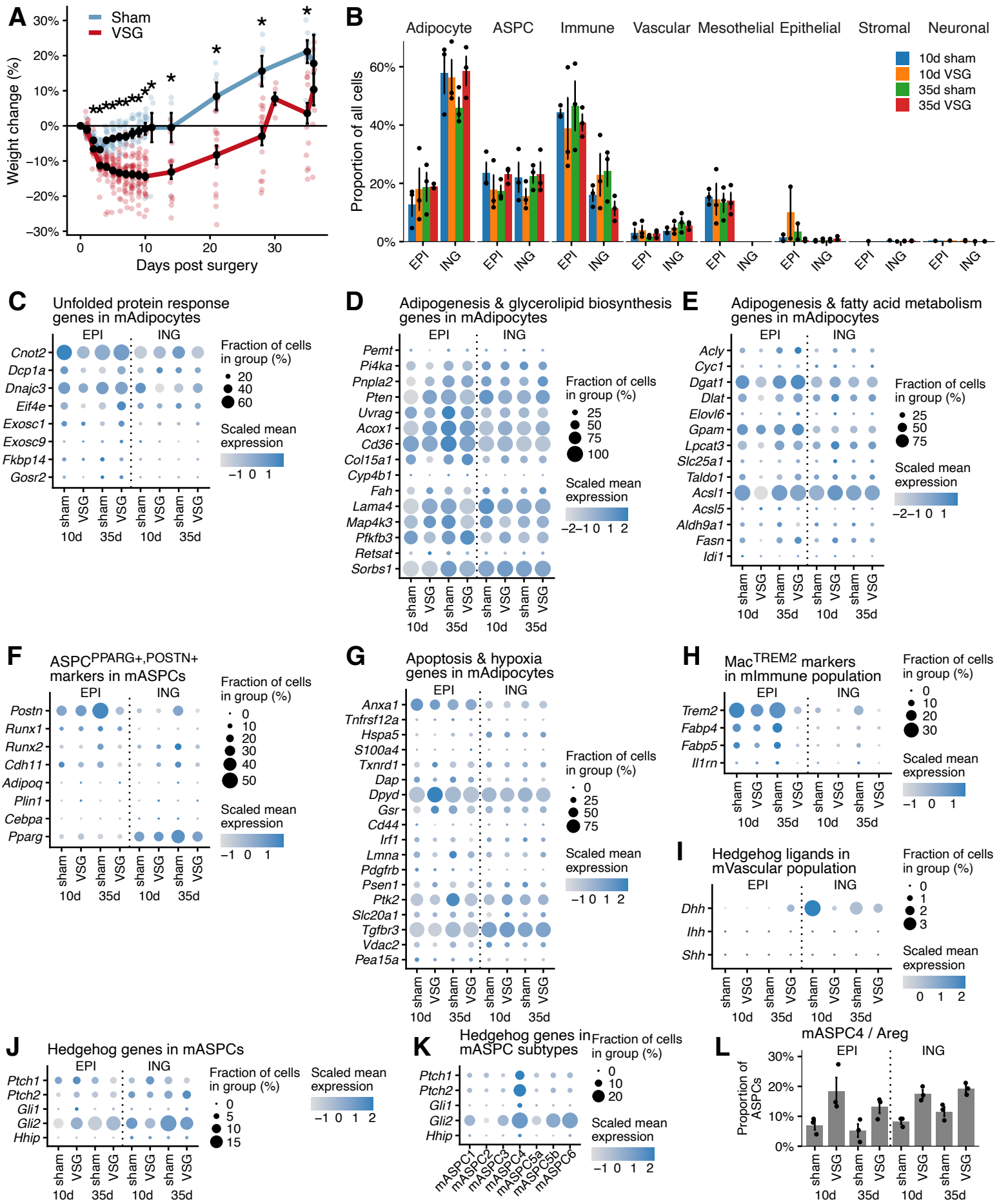
A
Sham
VSG
Weight change (%)
Days post surgery
B
Adipocyte
ASPC
Immune
Vascular
Mesothelial
Epithelial
Stromal
Neuronal
Proportion of all cells
10d sham
10d VSG
35d sham
35d VSG
EPI
ING
C
Unfolded protein response genes in mAdipocytes
Cnot2
Dcp1a
Dnajc3
Eif4e
Exosc1
Exosc9
Fkbp14
Gosr2
Fraction of cells in group (%)
Scaled mean expression
D
Adipogenesis & glycerolipid biosynthesis genes in mAdipocytes
Pemt
Pi4ka
Pnpla2
Pten
Uvrag
Acox1
Cd36
Col15a1
Cyp4b1
Fah
Lama4
Map4k3
Pfkfb3
Retsat
Sorbs1
E
Adipogenesis & fatty acid metabolism genes in mAdipocytes
Acly
Cyc1
Dgat1
Dlat
Elovl6
Gpam
Lpcat3
Slc25a1
Taldo1
Acsl1
Acsl5
Aldh9a1
Fasn
Idi1
F
ASPC PPARG+,POSTN+ markers in mASPCs
Postn
Runx1
Runx2
Cdh11
Adipoq
Plin1
Cebpa
Pparg
G
Apoptosis & hypoxia genes in mAdipocytes
Anxa1
Tnfrsf12a
Hspa5
S100a4
Txnrd1
Dap
Dpyd
Gsr
Cd44
Irf1
Lmna
Pdgfrb
Psen1
Ptk2
Slc20a1
Tgfbr3
Vdac2
Pea15a
H
Mac TREM2 markers in mImmune population
Trem2
Fabp4
Fabp5
Il1rn
I
Hedgehog ligands in mVascular population
Dhh
Ihh
Shh
J
Hedgehog genes in mASPCs
Ptch1
Ptch2
Gli1
Gli2
Hhip
K
Hedgehog genes in mASPC subtypes
mASPC1
mASPC2
mASPC3
mASPC4
mASPC5a
mASPC5b
mASPC6
L
mASPC4 / Areg
Proportion of ASPCs
sham
VSG
10d
35d

Supplemental Figure 1

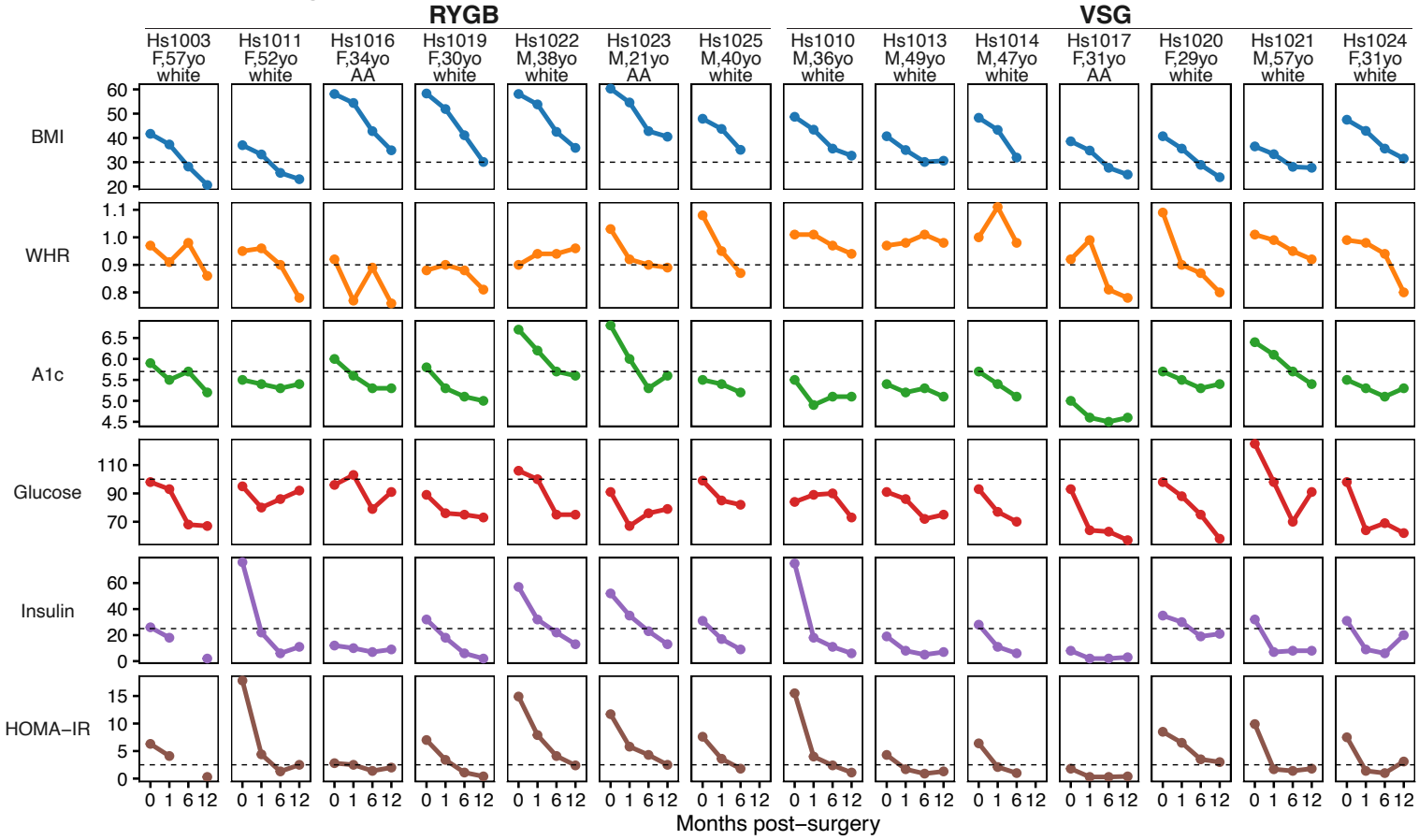

Supplemental Figure 2

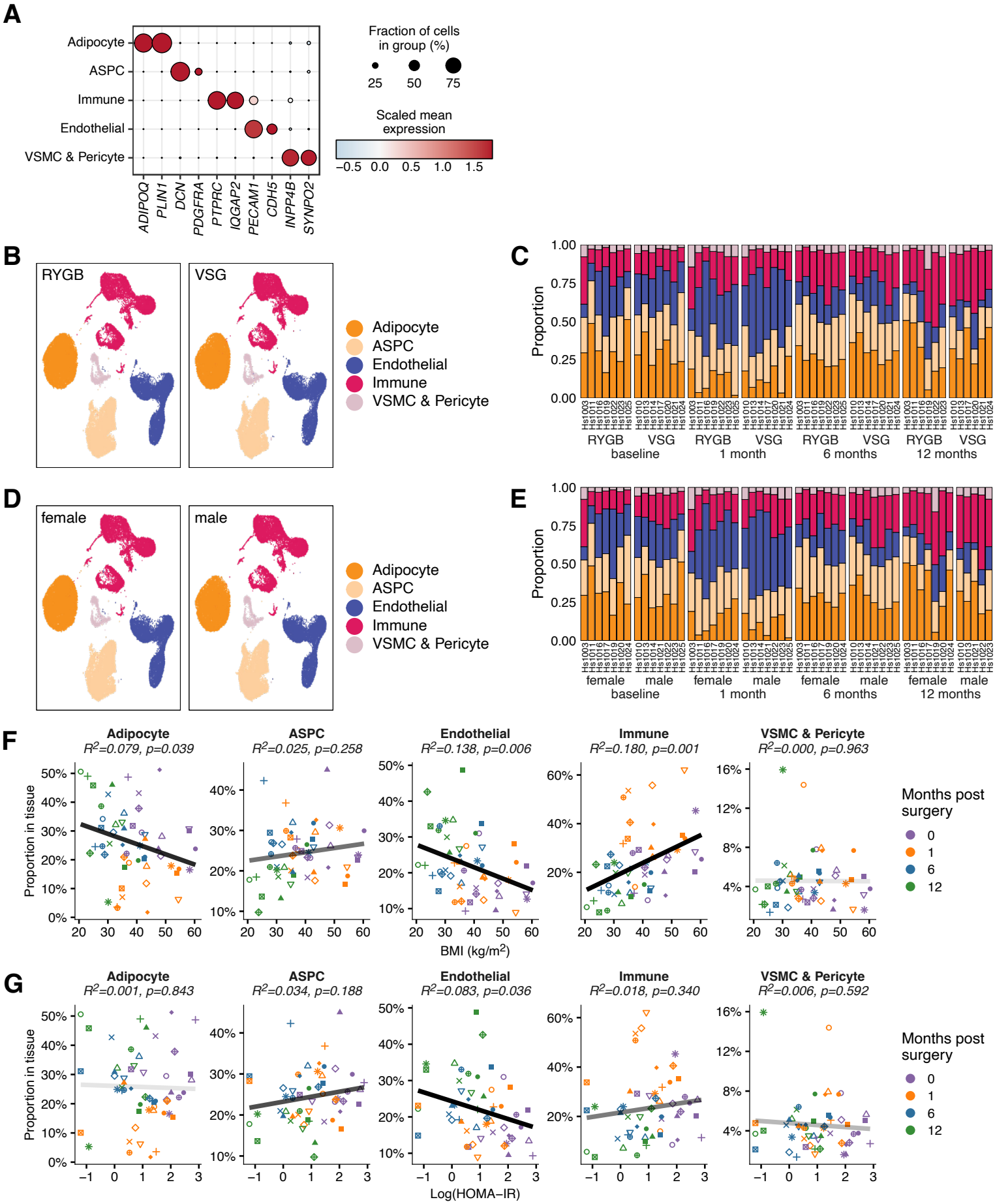

Supplemental Figure 3

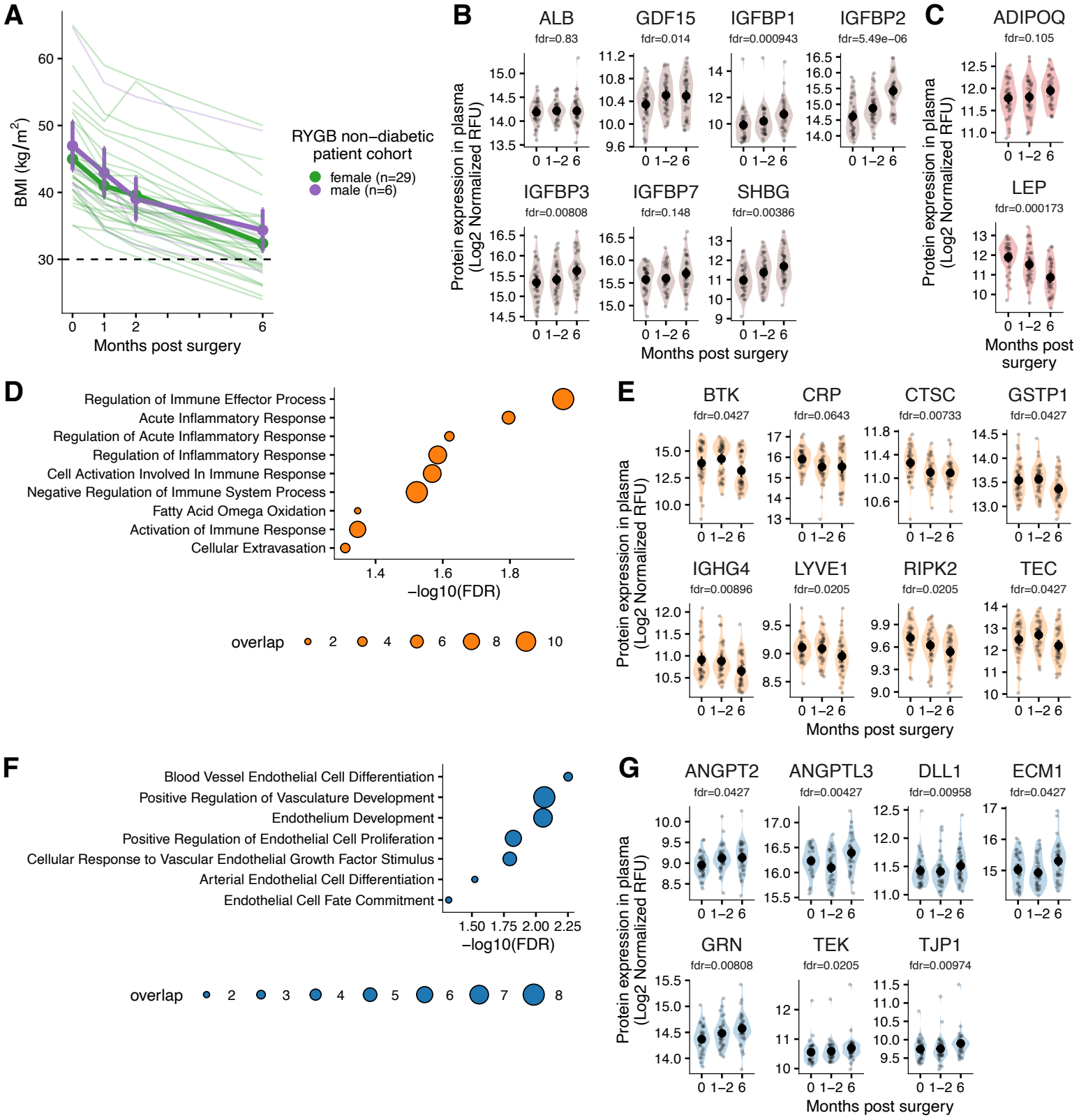

Supplemental Figure 4

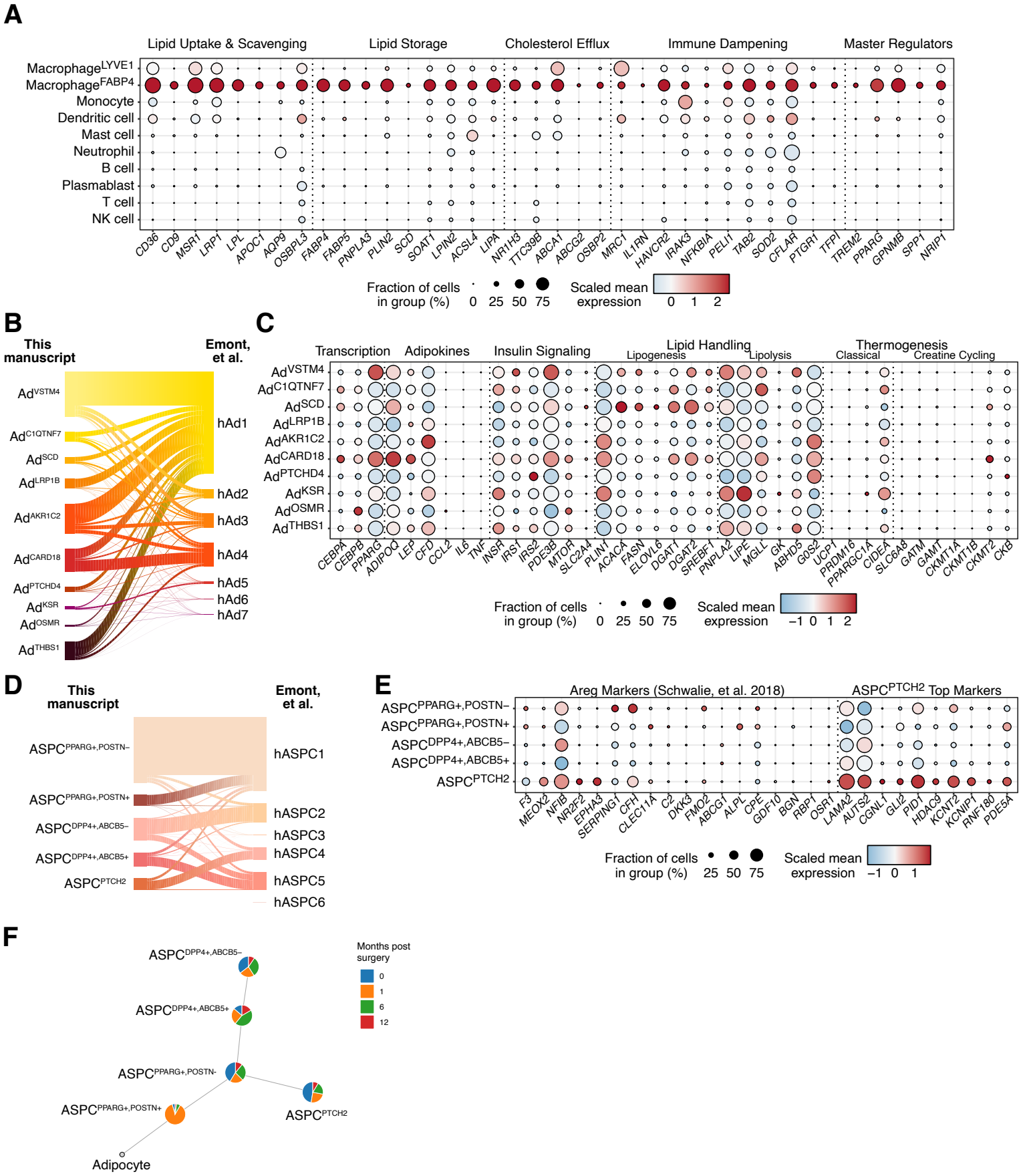

Supplemental Figure 5

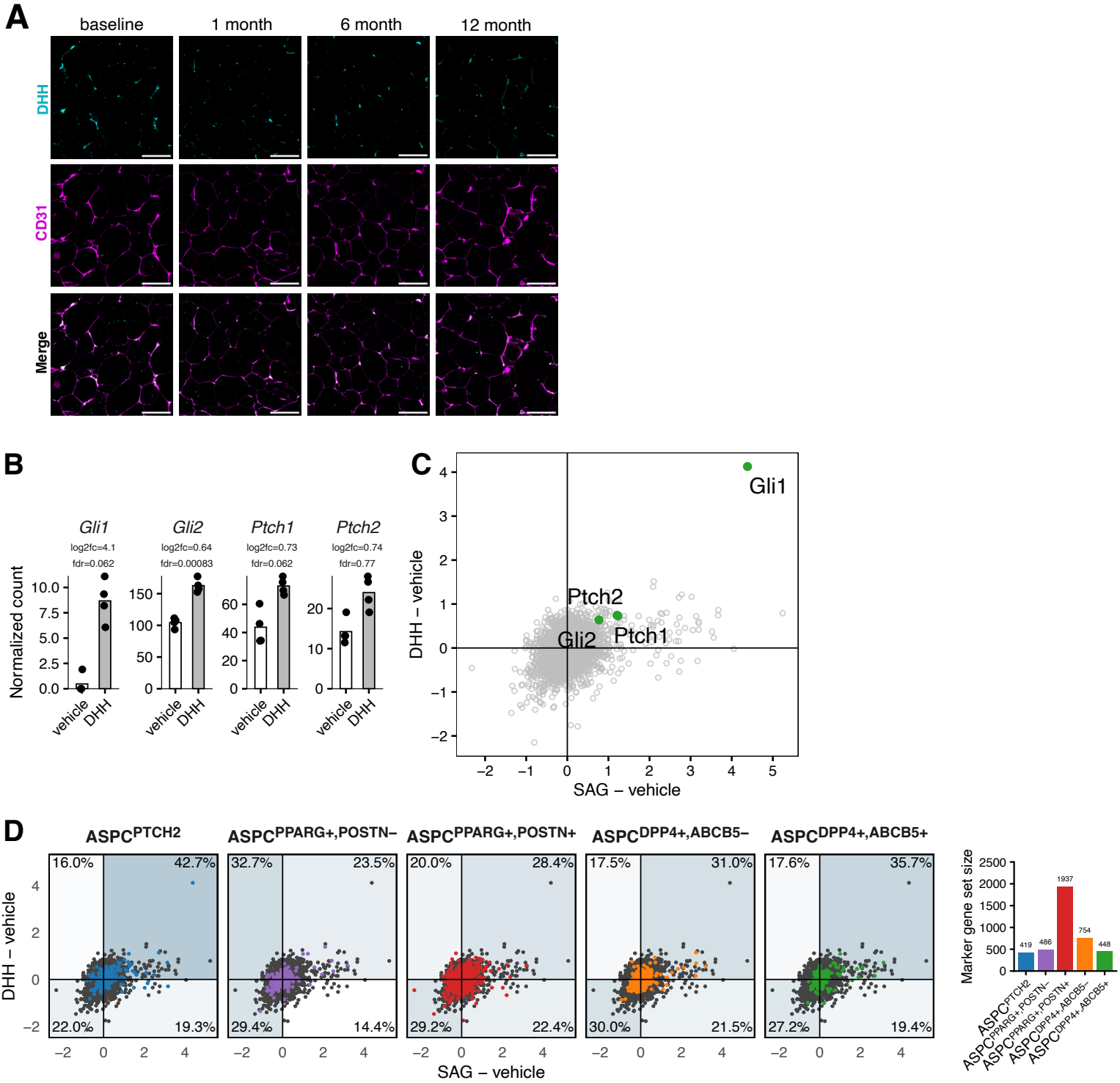
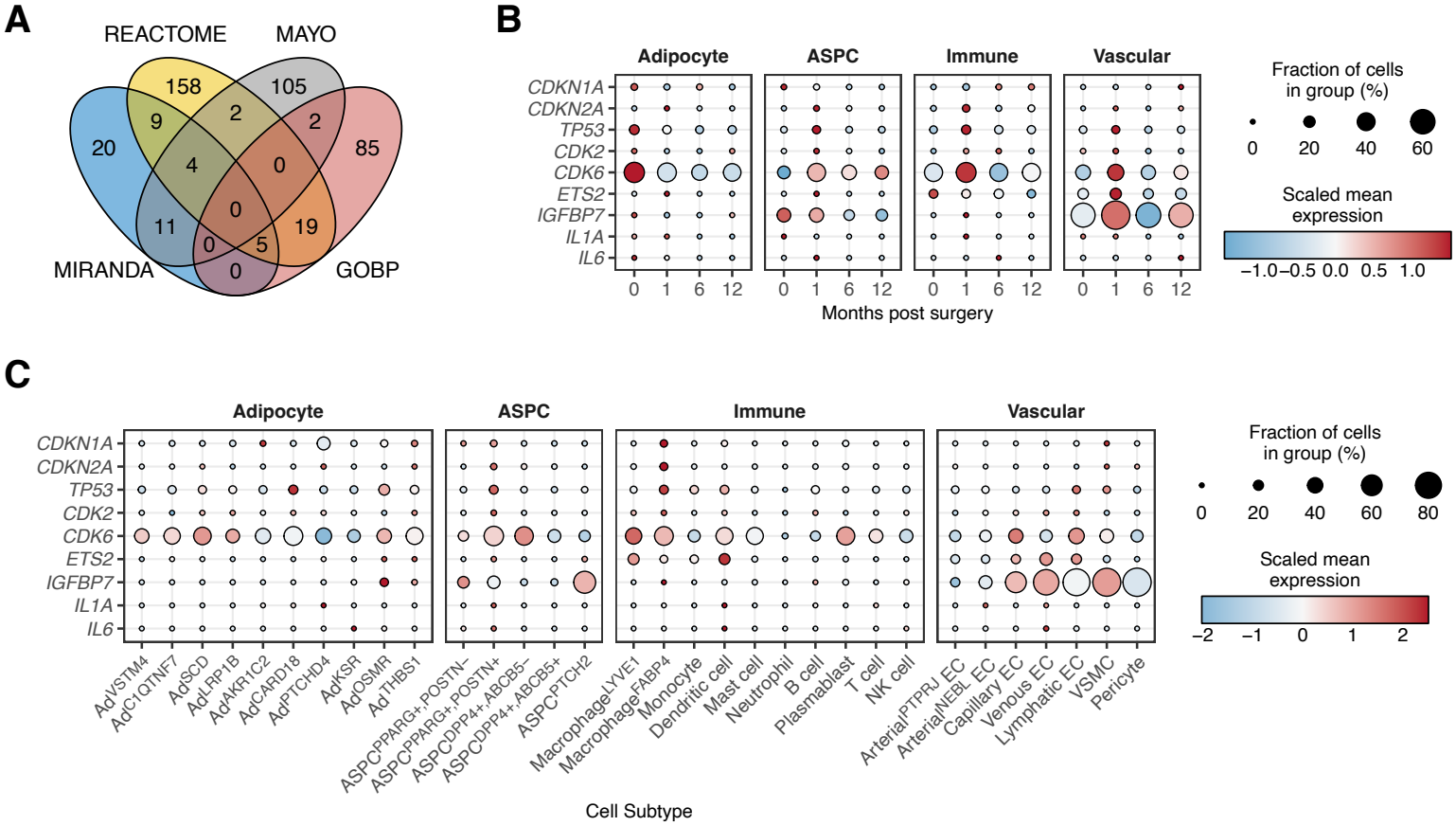
Supplemental Figure 6